UNIVERSIDAD DE INVESTIGACIÓN DE TECNOLOGÍA EXPERIMENTAL YACHAY

Escuela de Ciencias Físicas y Nanotecnología

TÍTULO: First-Principles Ultrafast Charge Carrier Dynamics of Methylammonium Lead Halide Perovskites

Trabajo de integración curricular presentado como requisito para la obtención de título de Físico

Autor:
Ariel M. Cabrera Aguilar

Tutor:
Prof. Dr. Henry P. Pinto

Co-tutor:
Prof. Dr Caterina Cocchi

Urcuquí, agosto, 2023

AUTORÍA

Yo, **Ariel Moises Cabrera Aguilar**, con cédula de identidad 1207659838, declaro que las ideas, juicios, valoraciones, interpretaciones, consultas bibliográficas, definiciones y conceptualizaciones expuestas en el presente trabajo; así cómo, los procedimientos y herramientas utilizadas en la investigación, son de absoluta responsabilidad de el/la autor (a) del trabajo de integración curricular. Así mismo, me acojo a los reglamentos internos de la Universidad de Investigación de Tecnología Experimental Yachay.

Urcuquí, agosto del 2023

Firmado electrónicamente por:
ARIEL MOISES
CABRERA
AGUILAR

Ariel Moises Cabrera Aguilar
CI: 1207659838

AUTORIZACIÓN DE PUBLICACIÓN

Yo, **Ariel Moises Cabrera Aguilar**, con cédula de identidad 1207659838, cedo a la Universidad de Investigación de Tecnología Experimental Yachay, los derechos de publicación de la presente obra, sin que deba haber un reconocimiento económico por este concepto. Declaro además que el texto del presente trabajo de titulación no podrá ser cedido a ninguna empresa editorial para su publicación u otros fines, sin contar previamente con la autorización escrita de la Universidad.

Asimismo, autorizo a la Universidad que realice la digitalización y publicación de este trabajo de integración curricular en el repositorio virtual, de conformidad a lo dispuesto en el Art. 144 de la Ley Orgánica de Educación Superior.

Urcuquí, agosto del 2023.

Firmado electrónicamente por:
ARIEL MOISES
CABRERA
AGUILAR

Ariel Moises Cabrera Aguilar
CI: 1207659838

Dedicatoria

Para *N* y *N*.

Ariel M. Cabrera Aguilar

Acknowledgements

I truly want to thank my mother. This work would not have been possible without her. She has been with me throughout the entire process of my academic journey, and I owe all of my successes to her. I love you, mom.

I want to thank Prof. Henry Pinto for believing in me, believing in my projects, and introducing me to this beautiful area of solid-state physics. I also want to thank the support of Prof. Dr. Caterina Cocchi and the 'Electronic Structure Theory' group from the University of Oldenburg has been invaluable to me. Not only did they help me make this project possible, but they also introduced me to a highly professional research environment.

Dear Cris, I do not love you as if you were a salt-roze, or topaz, or the arrow of carnations the fire shoots off. I love you as the plant that never blooms but carries in itself the light of hidden flowers. I love you without knowing how, or when, or from where. I love you straightforwardly, without complexities or pride; so I love you because I know no other way than this: so close that your hand on my chest is my hand,so close that when you close your eyes I fall asleep.

To my dear friend Negrita, I will never forget the day we met in Yachay. I miss you more than anything in this world.

Last but not least, to my dear friends Alfredo and Cecilia, I wish we had more time, as I have truly found sincere friendship in the both of you.

I think that sometimes the universe has strange ways of teaching you things. The key for me, and for many of us, is to never give up until you take your last breath. Life can bring a lot of challenges, but it can also bring amazing things. I have faith in that. There is no such thing as a painless lesson.
You can not gain anything without losing something first. Although, if you can endure that pain and walk away from it, you will find that you now have a heart strong enough to overcome any obstacle. Yes, a heart made FULLMETAL.

Ariel M. Cabrera Aguilar

Resumen

Los semiconductores de perovskita de haluro de plomo y metilamonio, $MAPbX_3$ (MA = CH_3NH_3, X= I, Br, Cl), se han convertido en el foco de los esfuerzos de investigación en el campo de la energía fotovoltaica. La investigación de procesos en un nivel de nanoescala se puede lograr a través de la teoría funcional de densidad dependiente del tiempo en tiempo real y la dinámica molecular de Ehrenfest. En un trabajo de primeros principios basado en la teoría funcional de densidad dependiente del tiempo en tiempo real, investigamos la dinámica ultrarrápida del portador de carga de $MAPbI_3$. Este trabajo también incluye cálculos ab initio de la teoría funcional de la densidad (DFT) sobre la estructura electrónica del uso de funcionales de última generación, incluidas las aproximaciones HSE06 y GW. Los resultados de la estructura electrónica confirman una alta localización del componente inorgánico de la perovskita cerca del nivel de Fermi. Se encontró que los cationes $CH_3NH_3^+$ no contribuyen a la absorción óptica, sino que actúan como un relleno estructural y aseguran la neutralidad de carga de la celda unitaria. La dinámica ultrarrápida de las perovskitas de haluro de plomo de metilamonio (X = I) se analizó siguiendo la evolución de la población de portadores de carga utilizando el formalismo de la teoría funcional de densidad dependiente del tiempo en tiempo real (TDDFT). El espectro de absorción calculado bajo el enfoque de aproximación de densidad local adiabática (ALDA) reproduce dos excitaciones de alta energía, que son consistentes con los resultados experimentales. Al incidir en el sistema con un pulso de femtosegundo coherente y con intensidades variables, se encontró una respuesta pronunciada dependiente de la intensidad, que se manifiesta en la generación de armónicos altos. De esta forma, se puede interpretar la dinámica del portador de carga en términos de estimadores simples, como el número de electrones excitados.

Palabras clave: DFT, methylammonium lead triiodide perovskites, ultrafast dynamics, time-dependent density functional theory

Abstract

Methylammonium lead halide perovskite semiconductors, $MAPbX_3$ (MA = CH_3NH_3, X= I, Br, Cl), have become the focus of research efforts in the field of photovoltaics. Investigating processes on a nanoscale level can be achieved through real-time time-dependent density functional theory and Ehrenfest molecular dynamics. In a first-principles work based on real-time time-dependent density-functional theory, we investigate the ultrafast charge-carrier dynamics of $MAPbI_3$. This work also includes ab initio density-functional theory (DFT) calculations on the electronic structure of using state-of-the-art functionals, including HSE06 and GW approximations. The electronic structure results confirm a high localization of the inorganic component of the perovskite near the Fermi level. It was found that the $CH_3NH_3^+$ cations do not contribute to the optical absorption but instead act as a structural filler and ensure the charge neutrality of the unit cell. The ultrafast dynamics of methylammonium lead halide perovskites (X = I) were analyzed by following the evolution of the charge-carrier population using the formalism of real-time time-dependent density-functional theory (TDDFT). The absorption spectrum calculated under the adiabatic local density approximation (ALDA) approach reproduces two high-energy excitations, consistent with experimental results. By irradiating the system with coherent femtosecond pulses at varying intensities, a pronounced intensity-dependent response was observed, manifested through high-harmonic generation. In this way, one can interpret the charge-carrier dynamics in terms of simple estimators, such as the number of excited electrons.

Keywords: DFT, methylammonium lead triiodide perovskites, ultrafast dynamics, time-dependent density functional theory

Contents

Acknowledgements **ix**

Resumen **xi**

Abstract **xiii**

List of Figures **xvii**

List of Tables **xix**

1 Introduction **1**
1.1 Problem Statement 1
1.2 General and specific objectives 2
1.3 Overview 2

2 Theoretical Background **3**
2.1 The time-independent Schrödinger equation 3
2.1.1 Solution schemes 4
Adiabatic Approximation 4
Mean Field Approximation 5
Hartree-Fock equations 6
2.2 The formal framework of density-functional Theory 7
2.2.1 The Hohenberg-Khon Theorem 7
2.2.2 The Khon-Sham equations 8
2.2.3 Functionals 8
The local density approximation (LDA) 8
The generalized gradient approximation (GGA) 9
The r^{2}SCAN functional 10
The HSE06 functional 11
2.3 The basic formalism of time-dependent DFT 11
2.3.1 Fundamental Theorems 12
The Runge-Gross Theorem 12
2.3.2 The time-dependent Kohn-Sham equations 13
2.3.3 The adiabatic local density approximation (ALDA) 14
2.3.4 Time-dependent current-DFT 14
2.3.5 Linear response theory in TDDFT 15
2.3.6 Laser Dynamics 16

2.4 The Vienna *ab initio* Simulation Package (VASP) . . . 17
2.5 The Octopus Code . . . 17
2.6 Methylammonium Lead Triiodide Perovskites . . . 18

3 Methodology **19**
3.1 Optimization of parameters . . . 19
3.1.1 VASP . . . 19
Structural relaxation . . . 21
3.1.2 Octopus . . . 22
Spacing and k-points . . . 22
TD calculations . . . 24

4 Results and Discussion **25**
4.1 Electronic structure analysis . . . 25
4.1.1 Density of states . . . 25
4.1.2 Band structure . . . 26
4.2 Linear Absorption Spectrum . . . 27
4.3 Ultrafast charge-carrier dynamics . . . 28
4.3.1 Induced electric current density . . . 28
4.3.2 Excitation energy . . . 29

5 Conclusions and future work **31**

A Data analysis **33**
A.1 Density of states . . . 33

Bibliography **35**

List of Figures

2.1 Atomic structure of the orthorhombic $CH_3NH_3PbI_3$ perovskite crystals. (a) The orthorhombic phase (space group *Pnma*) with optimized lattice parameters (experimental values in parentheses[76]): $a = 9.21$ (8.86) Å, $b = 8.86$ (8.58) Å, $c = 13.15$ (12.66) Å. (b) A side view of the δ phase of the $CH_3NH_3PbI_3$ perovskite. 18

3.1 Crystal structure of the orthorhombic phase (space group *Pnma*) $CH_3NH_3PbI_3$ perovskite crystal used as an initial input for the VASP calculations. 20
3.2 Convergence of the total energy with respect to the cutoff energy of the bulk structure in which a 1 mev/atom is achieved for a $E_{cut} = 850$ eV. 20
3.3 Energy convergence with respect to the k-poins mesh. The gray area represents the 1 meV/atom convergence range criteria. A $3 \times 2 \times 3$ 21
3.4 Computed 3^{th} order Birch-Murnagham EOS using r²SCAN+rVV10. 22
3.5 Energy convergence of the $MAPbI_3$ perovskite with respect to the spacing. The system reaches a converged value starting from 0.18Å. 23
3.6 Energy convergence of the $MAPbI_3$ perovskite with respect to the k-points. The system reaches a converged value starting from the $5 \times 3 \times 5$ k-points mesh. 24

4.1 Total density of states and partial density of states (PDOS) of an orthorhombic $CH_3NH_3PbI_3$ structure using the HSE06 functional (a) and the r²SCAN+rVV10 functional (b). 25
4.2 Calculated band structure of orthorhombic supercell of the $CH_3NH_3PbI_3$ perovskite along the high-symmetry lines in the first Brillouin zone using the LDA approximation (a) and the r²SCAN+rVV10 functional (b). 26
4.3 Absorption spectra of the $MAPbI_3$ perovskite structure for $\hat{\mathbf{x}}$ polarization direction (a), where we report two high energy peaks at E_1 and E_2. Absorption spectra (b) assuming different polarization directions along the x, y, and z axes. 27
4.4 Time evolution of the induced electric current density, $J(t)$, at varying intensities of the laser pulse, represented in black in the background: (a) $I = 6 \times 10^9$ W/cm^2, (b) $I = 1 \times 10^{10}$ W/cm^2, (c) $I = 1 \times 10^{11}$ W/cm^2, and (d) $I = 1 \times 10^{12}$ W/cm^2. 28
4.5 High-harmonic spectrum, $H(\omega)$, for the $MAPbI_3$ perovskite generated by pulses of increasing intensities. We displayed the fundamental carrier frequency (ω_0) and its overtones (ω_1 and ω_2). 29

4.6 Excitation energy $\Delta E_{ex}(t) = E(t) - E(t = 0)$ as a function of the laser intensity (a) with t = 40 fs and (b) within the entire temporal range. Number of excited electrons, $N_{ex}(t)$ (c) with t=40 fs and (d) within the entire temporal range. 30

A.1 Partial densoty of states of atoms in orthorhombic $CH_3NH_3PbI_3$ perovskite structures using the r^{2}SCAN+*r*VV10 functional. 33

List of Tables

3.1 Computed r²SCAN+*r*VV10 crystallographic data for the optimal unit cell of the $CH_3NH_3PbI_3$ perovskite and experimental data. 22

4.1 Summary of the main peaks appearing in the absorption spectrum of $MAPbI_3$ when varying the polarization direction of the Gauge field kick. 27

Chapter 1

Introduction

Because of the high absorption coefficients, low carrier recombination at the interfaces, low-cost fabrication processes[1], high short circuit current density (90% of internal quantum efficiency)[2], long-range carrier-diffusion lengths (100-100nm)[3], the photovoltaic absorber materials based on the $CH_3NH_3PbI_3$ perovskite ($MAPbI_3$) of the organo-lead halide type have proven to be strong candidates to construct highly efficient solar cells.

The potential applications of hybrid organic-inorganic perovskites in photovoltaics have been motivated by the continuous increase in high-efficiency rates[4–6]. The first demonstration of the operation of a hybrid perovskite solar cell was first shown by Kojima et al. using methylammonium lead iodide in 2009[7]. Theoretical investigations on the fundamental electronic properties of halide perovskites were done even before the first perovskite solar cell was reported[8,9]. Density-functional theory (DFT) is a computational modeling method to investigate many-body systems' electronic structure. This theory enables us to explore the properties of many-electron systems by employing various functionals, among which the exchange-correlation functional is an approximated quantity.

Describing the photoconversion properties and mechanisms is relevant for establishing high-performance solar cells. Based on various optical measurements, there is a strong consensus that band-to-band interactions predominantly govern photoabsorption and photoemission processes. Typically, the energy of incident photons equals the energy gap of an electron transition, resulting in a linear process. However, significantly higher energies can induce linear and nonlinear electronic and optical properties.

The transfer of energy via light irradiation with solid materials is one of the most fundamental interactions of great technological relevance [10]. Studying light induced electron dynamics in solids provides a microscopic idea of the highly-nonlinear phenomena, such as high order harmonic generation[11]. The capability of real-time time-dependent density functional theory (RT-TDDFT) to simulate the dynamics of charge carriers on their natural femtosecond timescale is a truly powerful technique for better understanding how these behaviors contribute to the formation of photoexcited electrons.

1.1 Problem Statement

Understanding the dynamic processes involved in laser perturbations in this material could enhance our comprehension of excitation processes in the femtosecond regime, which can now be revealed by the latest laser technologies. However, the successful manipulation of the $MAPbI_3$ perovskite through laser irradiation requires knowledge of the electronic structure and the microscopic mechanisms governing the coherent response of the system to the external ultrafast perturbation.

1.2 General and specific objectives

The general objective of this work is to perform *ab initio* simulations to uncover and analyze the relevant features in the electronic properties of the material. The initial analysis aims to establish a foundation for the subsequent examination of optical absorption. Following these calculations and the analysis of optical transitions, our goal is to derive specific observables that quantify the effects of an applied electric field on the system, including the number of excited electrons and the induced electric current density.

1.3 Overview

We conducted several simulations involving VASP and the Octopus codes in this research work. Details concerning each of these codes will be provided throughout the development of this thesis. Within the VASP calculations, we utilized hybrid and GGA functionals to reproduce some of the most fundamental properties of the methylammonium lead triiodide perovskite. On the other hand, Octopus allowed us to incorporate real-time time-dependent DFT within the adiabatic local density approximation, enabling us to excite the system with various perturbations. In this case, we considered two types of perturbations: a Gauge Field Kick and an x-polarized time-dependent electric field with a Gaussian envelope.

Chapter 2

Theoretical Background

The following section is intended to offer an in-depth theoretical overview to introduce the computational methods used throughout our work.

2.1 The time-independent Schrödinger equation

Understanding the physical properties of a solid is strongly correlated with the electronic structure of a N interacting nonrelativistic electrons system. Then, to solve the many-body problem of finding the ground state energy of this system, we solve the eigenvalue problem,

$$\hat{H}\Psi(\mathbf{r}_1, ..., \mathbf{r}_N; \mathbf{R}_1, ..., \mathbf{R}_M) = E\Psi(\mathbf{r}_1, ..., \mathbf{r}_N; \mathbf{R}_1, ..., \mathbf{R}_M) \tag{2.1}$$

to obtain the lowest eigenvalue for the Hamiltonian $\hat{H} = \hat{T} + \hat{V}$ that includes the kinetic energy $\hat{T}$ and potential energy $\hat{V}$ of the system . The many body wavefunction considers N electrons with coordinates $\mathbf{r}_1, \mathbf{r}_2, ..., \mathbf{r}_N$ and M nuclei with coordinates $\mathbf{R}_1, \mathbf{R}_2, ..., \mathbf{R}_M$. Furthermore, the probability of finding any electron at position $\mathbf{r}$ is given by $|\Psi(\mathbf{r}_1, ..., \mathbf{r}_N; \mathbf{R}_1, ..., \mathbf{R}_M)|^2$, and the electronic charge density within the material:

$$n(\mathbf{r}) = N \int |\Psi(\mathbf{r}, \mathbf{r}_2, \ldots, \mathbf{r}_N; \mathbf{R}_1, \ldots, \mathbf{R}_M)|^2 d\mathbf{r}_2 \ldots d\mathbf{r}_N d\mathbf{R}_1 \ldots d\mathbf{R}_M \tag{2.2}$$

The contributions to the kinetic energy of the many atoms system come from the kinetic energy of the electrons $\hat{T}_e$ and the nuclei $\hat{T}_n$[12]:

$$\hat{T} = \hat{T}_e + \hat{T}_n = -\sum_{i=1}^{N} \frac{\hbar^2}{2m_e}\nabla_i^2 - \sum_{I=1}^{M} \frac{\hbar^2}{2M_I}\nabla_I^2, \tag{2.3}$$

where $M_1, M_2, ..., M_M$ are the masses of the nuclei and m_e is the mass of the electron. The contribution to the potential energy $\hat{V}$ comes from the interaction between the electrically charged particles: the Coulomb repulsion interactions between pairs of electron $\hat{W}_{ee}$ and nuclei $\hat{W}_{nn}$, and the electron-nucleus $\hat{W}_{en}$ attractive interaction:

$$\hat{V} = \hat{W}_{ee} + \hat{W}_{nn} + \hat{W}_{en} = \frac{1}{2}\sum_{i \neq j}^{N} w\frac{1}{|\mathbf{r}_i - \mathbf{r}_j|} + \frac{1}{2}\sum_{I \neq J}^{M} w\frac{Z_I Z_J}{|\mathbf{R}_I - \mathbf{R}_J|} - \sum_{i,I} w\frac{Z_I}{|\mathbf{r}_i - \mathbf{R}_I|}, \tag{2.4}$$

where $w = e^2/4\pi\epsilon_0$. The e constant represents the electron charge, ϵ_0 is the vacuum permittivity, and $Z_{I,J}$ represents the atomic numbers. Combining all the described contributions, one can construct the full many-body Schrödinger equation:

$$\begin{aligned}\Bigg[&-\sum_{i=1} \frac{\hbar^2}{2m_e}\nabla_i^2 - \sum_{I=1}\frac{\hbar^2}{2M_I}\nabla_I^2 + \frac{1}{2}\sum_{i\neq j} w\frac{1}{|\mathbf{r}_i - \mathbf{r}_j|} + \ldots \\ &+\frac{1}{2}\sum_{I\neq J} w\frac{Z_I Z_J}{|\mathbf{R}_I - \mathbf{R}_J|} - \sum_{i,I} w\frac{Z_I}{|\mathbf{r}_i - \mathbf{R}_I|}\Bigg]\Psi = E_{tot}\Psi,\end{aligned} \tag{2.5}$$

where a rigorous description would also include relativistic corrections, external perturbations, and time dependence. The value of any physical observable $\hat{A}$ can be calculated from the expectation value $A_i = \langle \Psi_i | \hat{A} | \Psi_i \rangle$. For instance, we are interested in finding the lowest energy of an eigenstate in the system, which can be described by $E_0 = \langle \Psi_0 | \hat{H} | \Psi_0 \rangle$. The wave function can accurately describe the state of the system and the outcomes of any physical observables $\hat{A}$. However, obtaining the solution of the many-body Schrödinger equation is a numerical problem that grows exponentially with the size of the system[13]. Special cases exist in which solutions can be found for one and two-electron systems but with numerous conditions[14,15]. The following sections will show that several physical properties can be obtained without finding the exact solution to eqn 2.5.

2.1.1 Solution schemes

Several approximations have been developed since the 1920s (Fermi, 1927; Thomas, 1927; Hartree, 1928a, 1928b; Slater, 1929; Fock, 1930) in order to obtain a solution of eqn 2.5. Among these methods are the first quantitative cellular calculations done by the statistical description of the atomic properties based on the electronic density $n(\mathbf{r})$ done by the Born-Oppenheimer Approximation, the mean-field approximation, and the Hartree Fock theory.

Adiabatic Approximation

In solids, nuclei are located at approximate definite positions, and that causes the electrons to have a higher ratio of kinetic energy to potential energy. Furthermore, a significant difference of mass between the electrons and nuclei[16] (the mass of the proton is 1836 times bigger than the mass of the electron) indicates immediate re-adjustment of the low-energy state of the electrons[17]. These several ideas lead us to the conclusion that a good strategy might be decoupling the total wavefunction by including the only-electron, $\Psi_{\mathbf{R}}$, and the nuclear-only wavefunction χ :

$$\Psi\left(\mathbf{r}_1, \ldots, \mathbf{r}_N; \mathbf{R}_1, \ldots, \mathbf{R}_M\right) = \Psi_{\mathbf{R}}\left(\mathbf{r}_1, \ldots, \mathbf{r}_N\right)\chi\left(\mathbf{R}_1, \ldots, \mathbf{R}_M\right), \tag{2.6}$$

where one must remember that $\Psi_{\mathbf{R}}$ is defining a complete set of states for the electrons at each nuclear coordinate $\mathbf{R}$. Then, we can rewrite 2.5 by explicitly including the nuclear coordinates and neglecting the kinetic energy of the nuclei:

$$\left[-\sum_{i=1} \frac{\nabla_i^2}{2} + \frac{1}{2} \sum_{i \neq j} \frac{1}{|\mathbf{r}_i - \mathbf{r}_j|} + \sum_i \hat{W}_{en}(\mathbf{r}_i; \mathbf{R}) \right] \Psi_{\mathbf{R}} = E_{\mathbf{R}} \Psi_{\mathbf{R}} \tag{2.7}$$

On the other side, in order to find χ, use eqn 2.6 into 2.7 to obtain:

$$E_{\mathbf{R}} \Psi_{\mathbf{R}} \chi + \left[-\sum_{I=1} \frac{\nabla_I^2}{2M_I} + \frac{1}{2} \sum_{I \neq J} \frac{Z_I Z_J}{|\mathbf{R}_I - \mathbf{R}_J|} \right] \Psi_{\mathbf{R}} \chi = E_{tot} \Psi_{\mathbf{R}} \chi \tag{2.8}$$

Then, let us multiply each side of the equation by $\Psi_{\mathbf{R}}^*$, and integrate over the electron variables $\mathbf{r}$ to find the many-body Schrödinger equation of the nuclei[18]:

$$\left[-\sum_{I=1} \frac{\nabla_I^2}{2M_I} + \frac{1}{2} \sum_{I \neq J} \frac{Z_I Z_J}{|\mathbf{R}_I - \mathbf{R}_J|} + E(\mathbf{R}_1, \ldots, \mathbf{R}_M) \right] \chi = E_{tot} \chi \tag{2.9}$$

in which the effect of the electron is taken into account by acting as a potential. The decoupling of eqn 2.5 introduces the notion of the adiabatic electron-nuclear dynamics where no energy transfer occurs between the electrons and the nuclei[19].

Mean Field Approximation

The wave function of the N-electron system can be written as a product of N single-electron functions ϕ_i:

$$\Psi(\mathbf{r}_1, \mathbf{r}_2, \ldots, \mathbf{r}_N) = \phi_1(\mathbf{r}_1) \ldots \phi_N(\mathbf{r}_N), \tag{2.10}$$

where the electrons have individual probabilities $|\phi_i|^2$, and each ϕ_i satisfies the Schrödinger equation. This approximation implies a non-interaction regime between the electrons where each electron occupies an eigenstate starting from the lowest eigenvalue. Equation 2.12 must obey Pauli's exclusion principle, and that can only be satisfied by the introduction of a more complex expression that considers the determinant of such functions, the "Slater Determinants"[20]. Under this approximation and considering nuclei of infinite mass $M_I = \infty$, the electron density becomes $n(\mathbf{r}) = \sum_i |\phi_i(\mathbf{r})|^2$. The Hamiltonian for each electron,

$$\hat{H}_0(\mathbf{r}) = -\frac{1}{2} \nabla^2 + \hat{W}_{en}(\mathbf{r}) \tag{2.11}$$

where $\hat{W}_{en}(\mathbf{r})$ considers an overall Coulomb potential experienced by the electrons. Then, the Schrödinger equation for each electron i becomes:

$$\hat{H}_0(\mathbf{r}) \phi_i(\mathbf{r}) = \epsilon_i \phi_i(\mathbf{r}) \tag{2.12}$$

The basic idea of the mean-field approximation is introducing a classical potential to step into a somewhat interactive regime between the electrons[21]. Any distribution of electronic charge $n(\mathbf{r})$ can generate an electrostatic potential ρ:

$$\nabla^2 \rho(\mathbf{r}) = 4\pi n(\mathbf{r}), \tag{2.13}$$

where we can define the "Hartree Potential" $\hat{W}_H(\mathbf{r}) = -\rho(\mathbf{r})$, which is the energy of the electrons within the electrostatic potential $\rho(\mathbf{r})$. Considering that $\hat{W}_H(\mathbf{r})$ must satisfies $\nabla^2 \hat{W}_H(\mathbf{r}) = -4\pi n(\mathbf{r})$, the solution of this equation is:

$$\nabla^2 \hat{W}_H(\mathbf{r}) = -4\pi n(\mathbf{r}) \tag{2.14}$$

Now that the system also experiences a new potential component $\hat{W}_H(\mathbf{r})$, the full Schrödinger equation for each electron i becomes:

$$\left[-\frac{\nabla^2}{2} + \hat{W}_{en}(\mathbf{r}) + \hat{W}_H(\mathbf{r})\right] \phi_i(\mathbf{r}) = \epsilon_i \phi_i(\mathbf{r}) \tag{2.15}$$

The reason behind naming this "mean-field approximation" is that each electron experiences an average potential. However, there has been a reduction in the complexity of the original eqn 2.5, the consequences of introducing a classical approach are the coupling of 2.15 with the electron density, and the difficulty of accurately predicting physical properties of material[21].

Hartree-Fock equations

The introduction of this approximation converges to the use of the product wave function (eqn 2.6), and the variational approach to tackle very complex systems[20,22]. Implementing the 'variational principle' and considering the lowest energy quantum state Φ, the energy of this state is:

$$thisE = \int d\mathbf{r}_1 \ldots d\mathbf{r}_N \Psi^* \hat{H} \Psi = \langle \Psi | \hat{H} | \Psi \rangle \tag{2.16}$$

Then, the variational of the energy concerning the functions ϕ_i

$$\frac{\delta E}{\delta \phi_i} = 0, \tag{2.17}$$

where orthonormality is considered for each ϕ_i. Then, the *Hartree-Fock* equations:

$$\left[-\frac{\nabla^2}{2} + \hat{W}_{en}(\mathbf{r}) + \hat{W}_H(\mathbf{r})\right] \phi_i(\mathbf{r}) + \int d\mathbf{r}' V_X(\mathbf{r}, \mathbf{r}') \phi_i(\mathbf{r}') = \epsilon_i \phi_i(\mathbf{r}), \tag{2.18}$$

$$n(\mathbf{r}) = \sum_i |\phi_i(\mathbf{r})|^2, \tag{2.19}$$

$$\nabla^2 \hat{W}_H(\mathbf{r}) = -4\pi n(\mathbf{r}) \tag{2.20}$$

Several approximate solutions have been developed for the 'Hartree-Fock' (Self-consistent-field) approximation[23,24]; however, the nature of the exchange term and the issues for the calculations truly resembles the difference with the previously introduced approximations in terms of complexity[23]. Introducing this nonlocal potential requires a selfconsistent iteration, in which an initial guess of the total, 'Hartree', and exchange potential, and the states

ϕ_i is proposed. Each iteration begins by calculating the ϕ_i of the potentials, and then the potentials are updated from those ϕ_i. The objective is to stop the iteration process once an accuracy criterion has been achieved to determine a reasonable approximation of the ground state.

2.2 The formal framework of density-functional Theory

2.2.1 The Hohenberg-Khon Theorem

The Hohenberg-Khon (HK) theorem represents the starting point for describing a theory of many-body systems characterized by the ground state density[25]. The ground state density is:

$$\begin{aligned} n_0(\mathbf{r}) &= \langle \Phi_0 | \hat{n}(\mathbf{r}) | \Psi_0 \rangle \\ &= N \sum_{\sigma_1,\ldots,\sigma_N} \int d^3r_2 \ldots d^3r_N |(\mathbf{r}\sigma_1, \mathbf{r}_2\sigma_2 \ldots \mathbf{r}_N\sigma_N | \Phi_0\rangle|^2 \end{aligned} \tag{2.21}$$

where the σ_i is the spin projection of the i particle along the z-direction. The statements that justify the HK theorem:

1. Let's consider the set of external potentials V, the set of resulting ground states G, and the set N of all ground state densities obtained through eqn 2.21. Considering the map $A : V \longrightarrow G$, and the map $M : G \longrightarrow N$, it can be stated that there is a one-to-one correspondence between the external potential W_{ext}, the ground state $|\Phi_0\rangle$, and the ground state density n_0:

   $$W_{ext}(\mathbf{r}) \Longleftrightarrow |\Psi_0\rangle \Longleftrightarrow n_0(\mathbf{r}) \tag{2.22}$$

   and the electron density determines uniquely the external potential W_{ext} in the ground state. Therefore, the external potential is an unique functional of the ground-state density, denoted as $\Psi[n]$.

2. Any physical property of the many-body system for ground and excited states is a density functional:

   $$O[n] := \langle \Psi[n] | \hat{O} | \Psi[n] \rangle \tag{2.23}$$

   For the ground state, the energy functional:

   $$E[n] := \langle \Psi[n] | \hat{H} | \Psi[n] \rangle = F[n] + \int d^3r W_{ext}(\mathbf{r}) n(\mathbf{r}) \tag{2.24}$$

   which has been described in terms of the density $n(\mathbf{r})$ and any external potential W_{ext}.

3. For any particular potential, we can define a global minimum for $E[n]$

   $$E[n_0] < E[n_0'] \Longleftrightarrow E_0 = \min_{n \in N} E[n] \tag{2.25}$$

   where the domain of this functional is restricted to ground state densities in N. In other words, the functional has been minimized by the ground state density $n_0(\mathbf{r})$ only.

Formal proof can be done on the first statement by *reductio ad absurdum*, leading to a contradiction. This can be done by assuming that $|\Psi_0\rangle$ is the ground state for two different potentials W_{ext}[25].

2.2.2 The Khon-Sham equations

The Hohenberg-Khon theorem leaves a new framework to obtain the total energy of the many-body system through a functional; however, the exact expression of this functional is still unknown, but many approximations have been developed throughout the years. Let us consider eqn 2.24 to split the functional $F[n]$ that is accounting for the kinetic and Coulomb energy, and an extra term $E_{xc}[n]$ which is called the exchange and correlation energy:

$$E = F[n] = \int d\mathbf{r} n(\mathbf{r}) V_n(\mathbf{r}) - \sum_i \int d\mathbf{r} \phi_i^*(\mathbf{r}) \frac{\nabla^2}{2} \phi_i(\mathbf{r}) + \frac{1}{2} \int \int d\mathbf{r} d\mathbf{r}' \frac{n(\mathbf{r}) n(\mathbf{r}')}{|\mathbf{r} - \mathbf{r}'|} + E_{xc}[n], \quad (2.26)$$

where the equation includes the external potential, the kinetic energy, the Hartree energy, and the exchange-correlation energy. Then, considering the global minimum energy for the energy functional $E[n]$ and the variational principle, the exchange-correlation potential can be defined as:

$$V_{xc}(\mathbf{r}) = \left. \frac{\delta E_{xc}[n]}{\delta n} \right|_{n(\mathbf{r})} \quad (2.27)$$

Then, the *Khon-Sham equations*:

$$\left[-\frac{\nabla^2}{2} + \hat{W}_{en}(\mathbf{r}) + \hat{W}_H(\mathbf{r}) \right] \phi_i(\mathbf{r}) + \int d\mathbf{r}' V_{xc}(\mathbf{r}, \mathbf{r}') \phi_i(\mathbf{r}') = \epsilon_i \phi_i(\mathbf{r}), \quad (2.28)$$

which are the equations that define the basis of the Kohn-Sham theory.

2.2.3 Functionals

Although the several approximations and the introduction of the exchange-correlation energy set up the basis of the most successful and robust calculations that we do today, there are still many challenges to overcome regarding the different approximate functionals that have been developed (range of interactions, self-interaction errors (SIEs), numerical accuracy). This section introduces the main characteristics, theory, and considerations for the widely-used functionals[26]. It will be seen that as we go to a high-accuracy regime, the computational cost increases. This can be visually represented as rungs on Jacob's ladder of sophistication[27]. The attention of this section will be focused on the adiabatic local density approximation (ALDA)[28], the r^{2}SCAN functional[29], and the HSE06 hybrid functional[30].

The local density approximation (LDA)

The basic idea behind this approximation is that at every point $\mathbf{r}$ in space, it considers the exchange-correlation energy density e_{xc} that we would obtain if we consider a homogeneous electron liquid with a $n(\mathbf{r})$ everywhere, in which we are considering an unpolarized system that considers the density of the spin densities as $n(\mathbf{r})/2$:

$$E_{xc}^{LDA}[n] = \int d^3 r e_{xc}^{ho}(\overline{n})\bigg|_{\overline{n}=n(\mathbf{r})} \tag{2.29}$$

Then, the exchange-correlation potential becomes.

$$v_{xc}^{LDA}(\mathbf{r}) = \frac{de_{xc}^{ho}(\overline{n})}{d\overline{n}}\bigg|_{\overline{n}=n(\mathbf{r})} \tag{2.30}$$

The approximate description fails when the many-body system presents non-uniform density regions. In other words, having slow changes in the density allows the LDA approximation to work better. This approximation works surprisingly better than other approximations (such as HF) and has provided accurate predictions of many physical properties. These approximations also present shortcomings, such as SIEs[31]. One would usually consider the spin densities within the local spin density approximation (LSDA), in which:

$$E_{xc}^{LSDA}[n_\uparrow, n_\downarrow] = \int d^3 r e_{xc}^{ho}(n_\uparrow(\mathbf{r}), n_\downarrow(\mathbf{r})) \tag{2.31}$$

This approximation locates on the first rung of Jacob's ladder, and its validity will be determined if the electron density of an electron liquid is enough to capture the complexity of many of the physical behaviors a system could present. Because the proposed local potential satisfies the sum rules and scaling properties, the approximation can find accurate predictions of the properties of materials, which would explain the success of this approach[32].

The generalized gradient approximation (GGA)

Let us now consider the next by removing the locality approach and consider a functional of the magnitude of the gradient of the density $|\nabla n^\sigma|$ and the value of n at each point. Then, the energy density at a point $\mathbf{r}$ can be expressed as the following functional:

$$E_{xc}^{GGA}[n] = \int d^3 r e_{xc}^{GGA}(n, |\nabla n^\sigma|), \tag{2.32}$$

where the objective is not to construct full analytical expressions but rather to find an approximation to the gradient expression series. Although the GGA could behave worse than LDA because it does not satisfy the sum rules[33], and the expansion can not characterize the large gradients in real materials. Within the gradient expansion approximation, one can construct density functionals in powers of gradients using a reduced gradient density:

$$s(\mathbf{r}) = \frac{\nabla n(\mathbf{r})}{2n(\mathbf{r})k_F(\mathbf{r})}, \tag{2.33}$$

where $k_F(\mathbf{r})$ is the local Fermi wave vector. A common approach to construct e_{xc}^{GGA} is to propose functions that could satisfy most of the properties of $e_{xc}[n]$, and several GGAs with several improvements and corrections have been proposed throughout the years, such as PBEsol[34] resulting in accurate lattice parameters with overestimated absorption energies, and BLYP[35] and PBErev[36] with large enhancement factors. The exchange functional of Becke (B88-1998)[35]can be introduced as:

$$E_x^{B88}[n_\uparrow, n_\downarrow] = E_x^{LSDA}[n_\uparrow, n_\downarrow] - \beta \sum_\sigma \int d^3 r n_\sigma^{4/3} \frac{x_\sigma^2}{1 + 6\beta x_\sigma sinh^{-1}(x_\sigma)} \tag{2.34}$$

where $x_\sigma = |\nabla n_\sigma(\mathbf{r})|/n_\sigma^[4/3](\mathbf{r})$ and β is an empirical parameter. Structuring a strategy to define which functional can truly contribute to predicting the properties of a material is a difficult task that can even require some experience[37]. Many of the efforts previously done are combined within the PBE functional[38]:

$$E_x^{PBE}[n] = \int d^3 r e_x^h(n) \left[1 + \kappa - \frac{\kappa}{1 + \beta\pi^2 s^2/3\kappa}\right] \tag{2.35}$$

Although PBE offers high accuracy in determining the structural properties of materials, it might fail to predict electronic properties.

The r²SCAN functional

Beyond the GGA approximation, it comes to the meta-GGA functionals that include orbital kinetic energy densities and particle density. Then, the exchange-correlation energy in meta-GGAs includes:

$$E_x^{PBE}[n] = \int d^3 r e_{xc}^{MGGA}(n_\uparrow(\mathbf{r}), n_\downarrow(\mathbf{r}), \nabla n_\uparrow(\mathbf{r}), \nabla n_\downarrow(\mathbf{r}), \nabla^2 n_\uparrow(\mathbf{r}), \nabla^2 n_\downarrow(\mathbf{r}), \tau^\uparrow, \tau^\downarrow) \tag{2.36}$$

Therefore, the next rung on the ladder of approximations includes the kinetic energy densities, which can be written as:

$$\tau^\sigma(\mathbf{r}) = \frac{1}{2}\sum_{i=1}^{N} |\nabla \psi_i^\sigma(\mathbf{r})|^2, \tag{2.37}$$

where the spin σ has been included explicitly. Considering that there is no unique expression for τ^σ,

$$\tau^\sigma(\mathbf{r}) = \tau_n^\sigma(\mathbf{r}) + \tau_x^\sigma(\mathbf{r}), \tag{2.38}$$

one can separate it into two expressions, where $\tau_x^\sigma(\mathbf{r})$ expresses the relative kinetic energy of the pair of electrons, and the nonuniqueness coming from the $\tau_n^\sigma(\mathbf{r})$ represents a more physical quantity because it involves the density $n^\sigma(\mathbf{r})$ and its derivatives.

The strongly constrained and appropriately normed (SCAN) functional has been highly successful in determining constraints (uniform and slowly varying densities, jellium surface energy, the $Z \longrightarrow \infty$ limit of the two-electron ion) from empirical considerations compared to the already introduced PBE functional[36]. The SCAN functional can be constructed in terms of the following variable:

$$\alpha(\mathbf{r}) = \frac{\tau_x^\sigma(\mathbf{r})}{\tau^{unif}(n(\mathbf{r}))} \tag{2.39}$$

where $\tau^{unif}(n(\mathbf{r}))$ is the kinetic energy density of the electron gas with density $n(\mathbf{r})$. This meta-GGA functional has proven to be highly successful among different systems, such as metal oxides[39], in silicon phases[40], and in high-temperature semiconductors[41].

The HSE06 functional

The next level of sophistication incorporates an explicit orbital functional, similar to the one introduced in eqn 2.37:

$$e_x^{exact}(\mathbf{r}) = -\frac{1}{2}\sum_{\sigma}\sum_{i,j=1}^{N_\sigma}\int d^3r' \frac{\phi_{i\sigma}^*(\mathbf{r}')\phi_{j\sigma}(\mathbf{r}')\phi_{i\sigma}(\mathbf{r})\phi_{j\sigma}^*(\mathbf{r})}{|\mathbf{r}-\mathbf{r}'|}, \tag{2.40}$$

where the xc functionals that depend on e_x^{exact} are known as hyper-GGAS. The basic idea behind the hybrid functionals is to mix the exact exchange functional with a standard GGA, in the following way:

$$E_{xc}^{hybrid} = aE_x^{exact} + (1-a)E_x^{GGA} + E_c^{GGA}, \tag{2.41}$$

where many hybrid functionals have been developed[42]. For instance, the B3LYP functional uses the Becke[35] exchange functional and the LYP[43] correlation:

$$E_{xc}^{B3LYP} = (1-a)E_x^{LDA} + aE_x^{exact} + bE_x^{B88} + cE_x^{LYP} + (1-c)aE_c^{LDA} \tag{2.42}$$

This functional is extremely popular because it surpasses other GGAs and meta-GGAs when predicting molecule properties. In solids, it fails to describe the homogeneous electron gas exactly[44]. The Coulomb interaction can be divided into two main contributions to treat different regions of the electron density with higher accuracy. Then, the short-range and long-range parts:

$$\frac{1}{\mathbf{r}-\mathbf{r}'} = \frac{f(\mu|\mathbf{r}-\mathbf{r}'|)}{\mathbf{r}-\mathbf{r}'} + \frac{1-f(\mu|\mathbf{r}-\mathbf{r}'|)}{\mathbf{r}-\mathbf{r}'}, \tag{2.43}$$

where the function f satisfies that $f(\mu x \to 0) = 1$ and $f(\mu x \to \infty) = 0$, and μ is usually called the range parameter. Then, the range-separated hybrid xc functional can have the following form:

$$E_{xc} = E_{XC}^{DFT} + a(E_x^{HF-SR} - E_x^{DFT-SR}) + b(E_x^{HF-LR} - E_x^{DFT-LR}) \tag{2.44}$$

One of the most popular options for solids is the Heyd–Scuseria–Ernzerhof range-separated hybrid functional HSE06[45], where the range parameter is chosen to be $0.11/a$.

2.3 The basic formalism of time-dependent DFT

This section introduces the basic principles of time-dependent density functional theory (TDDFT), which has emerged as a powerful theory to understand the time evolution of electronic many-body systems[46]. To approach the problem of resolving the time-dependent nature of processes involving the excited states of a system, the eqn. 2.5 must be transformed to the time-dependent Schrödinger equation in order to consider N interacting nonrelativistic fermions in an external potential $\hat{v}_{ext}(t)$. Then, the total Hamiltonian is:

$$\hat{H}(t) = \hat{T} + \hat{V}(t) + \hat{W}_{ee}(t) \tag{2.45}$$

Similar to eqns. 2.3 and, the kinetic energy and the particle-particle interaction terms are, respectively:

$$\hat{T} = -\frac{1}{2}\sum_{i=1}^{N}\nabla_i^2, \quad \text{and} \quad \hat{W}_{ee} = \frac{1}{2}\sum_{i\neq j}^{N}\frac{1}{|\mathbf{r}_i - \mathbf{r}_j|} \tag{2.46}$$

The time-dependent potential is given by

$$\hat{V}_{ext}(t) = \sum_{i=1}^{N} v_{ext}(\mathbf{r}_i, t), \tag{2.47}$$

where this expression represents the attraction of the electrons with the nuclei and the perturbation applied due to any field. Then, the time evolution of the system is governed by the time-dependent Schrödinger equation,

$$i\frac{\partial}{\partial t}\Psi(\mathbf{x}_1,\ldots,\mathbf{x}_N;t) = \hat{H}(t)\Psi(\mathbf{x}_1,\ldots,\mathbf{x}_N;t) \tag{2.48}$$

which has to be solved for a given initial state at t_0. The following sections shall put the most important aspects of the TD theory on a firm footing to understand many of the calculations that were done in this work.

2.3.1 Fundamental Theorems

The Runge-Gross Theorem

The theorem that forms the basis for the theory of TDDFT was first developed by Runge and Gross in 1984[46], and it states:

- There is a one-to-one correspondence between the set of all TD external potentials $v_{ext}(\mathbf{r}, t)$, and the time-dependent densities $n(\mathbf{r}, t)$ from a fixed initial state Ψ_0:

  $$v_{ext}(\mathbf{r}, t) \xrightarrow[i\partial_t\Psi = \hat{H}(t)\Psi]{\Psi_0} \Psi(t) \xrightarrow{\langle\Psi(t)|\hat{n}|\Psi(t)\rangle} n(\mathbf{r}, t), \tag{2.49}$$

  within the time interval $t_0 < t < t'$. In principle, if one can determine the time-dependent density of the system, the external potential and the Hamiltonian can be determined, and all the properties of the system can be obtained by solving the TD Schrödinger equation. The proof of this theorem should show that the density $n(\mathbf{r}, t)$ is a variable that can determine the system's dynamics. In other words, it can be shown that two densities $n(\mathbf{r}, t)$ and $n'(\mathbf{r}, t)$ under the influence of two different potentials v_{ext} and v'_{ext} will always become different later than t_0 if the two different potentials differ by more than a time-dependent function $v(\mathbf{r},t) - v(\mathbf{r}',t) \neq a(t)$. Then, considering a fixed initial state Ψ_0:

$$n(\mathbf{r},t) \longleftrightarrow v_{ext}(\mathbf{r},t) + \Psi(t) \tag{2.50}$$

where $\Psi(t)$ is an unique functional of $n(\mathbf{r},t)$ up to some phase.

- Considering Frenkel's variational principle, the exact TD density can be found:

$$A[n] = \int_{t_0}^{t_1} dt \langle \Psi[n](t) | i\hbar\partial_t - \hat{H}'(t) | \Psi[n](t) \rangle, \tag{2.51}$$

where $\hat{H}'$ can be obtained by considering $v'_{ext}(\mathbf{r},t) = v_{ext}(\mathbf{r},t) + \partial_t \alpha(t)$, with the global phase $\alpha(t)$. Equation 2.51 becomes stationary for the correct td density $n(\mathbf{r},t)$, and we can consider the variational equation:

$$\frac{\delta A[n]}{\delta n(\mathbf{r},t)} = 0 \tag{2.52}$$

can be a relation equivalent to the TD Schrödinger equation, which comes from the equivalence with eqn. 2.27.

2.3.2 The time-dependent Kohn-Sham equations

Considering section two of the Runge and Gross Theorem[47], one can define the time-dependent Schrödinger equation of the form:

$$i\hbar \frac{\partial |\Phi[n](t)\rangle}{\partial t}, \tag{2.53}$$

where Φ is a functional of the density. Let us construct a noninteracting system with initial state ϕ_0. In order to measure the non-interactive system that will have the same evolution as the interactive one. Then the time-dependent density of the noninteracting system:

$$n(\mathbf{r},t) = \sum_j f_j |\phi_j(\mathbf{r},t)|^2, \tag{2.54}$$

where f_j is the orbital occupation, and the phi_j^0 N Kohn-Shan orbitals can construct the total initial noninteracting wave function Φ_0. These orbitals represent a self-consistent solution of the time-dependent Khon-Sham equations:

$$\hat{H}^{KS}[n](t)\phi_j(\mathbf{r},t) = i\hbar\partial_t \phi_j(\mathbf{r},t) \tag{2.55}$$

The Kohn-Sham Hamiltonian $\hat{H}^{KS}[n](t)$ includes the noninteracting kinetic energy, the time-dependent external potential of the system $v(\mathbf{r},t)$, the time-dependent Hartree potential $v_H(\mathbf{r},t)$, and the time-dependent xc potential $v_{xc}[n](\mathbf{r},t)$, respectively:

$$\hat{H}^{KS}[n](t) = -\frac{\nabla^2}{2} + v(\mathbf{r},t) + \int d^3r' \frac{n(\mathbf{r}',t)}{|\mathbf{r}-\mathbf{r}'|} + v_{xc}[n](\mathbf{r},t) \tag{2.56}$$

These TDKS equations set up a formalism to obtain the exact density of the many-body system from a ground state associated with $v_0(t)$. Several approaches, considerations, and approximations have to be made in order to solve these equations[48,49], but we will focus on the linear response theory in the adiabatic local density approximation (ALDA).

2.3.3 The adiabatic local density approximation (ALDA)

Accurate approximations must be made to the $v_{xc}[n](\mathbf{r},t)$ to get suitable descriptions of a system and one of these methodologies is to consider the description of xc functionals in stationary DFT with the actual td density of the system[50,51]. Then, in the ALDA approximation, the time-dependent xc potential is:

$$v_{xc}^{ALDA}(\mathbf{r},t) = \frac{\delta A_{xc}^{ALDA}[n]}{\delta n(\mathbf{r},t)} = \left.\frac{de_{xc}^{HEG}(n)}{dn}\right|_{\overline{n}=n(\mathbf{r},t)}, \tag{2.57}$$

where e_{xc}^{HEG} is the xc energy of a homogeneous electron liquid of particle of density n. We are limited by the information contained in $n(\mathbf{r},t)$ at a specific time t. Then, by considering effects coming from causal evolution only, we are restricted in a way with no memory effects[52]. The accuracy of the ALDA approximation has been questioned; however, it remains a powerful method to predict the behavior of many-body systems to TD perturbations.

2.3.4 Time-dependent current-DFT

The Runge-Gross Theorem sustaining the formalism of TDDFT is applicable to capture the response of systems like isolated atoms or molecules. However, the existence theorems do not hold when applied to periodic solids[53,54]. This comes from the fact that it is a requirement for the currents to vanish at infinity, and unfortunately, this does not apply to uniform electric fields in periodic systems. Additionally, since we are restricted to time-dependent scalar potentials, one can not consider vector potentials like time-dependent magnetic fields or the interaction of electromagnetic waves with matter. However, one can eliminate these requirements if the framework of time-dependent current-DFT (TDCDFT) is invoked[55]. Then, taking into account the formalism proposed by Vignale[55], let us consider the following Hamiltonian

$$\hat{H}(t) = \sum_{j=1}^{N}\left\{\frac{1}{2}\left[\frac{\nabla_j}{i} + \mathbf{A}(\mathbf{r}_j,t)\right]^2 + v(\mathbf{r}_j,t)\right\} + \frac{1}{2}\sum_{i,j\neq i}^{N} w(\mathbf{r}_i - \mathbf{r}_j), \tag{2.58}$$

where $v(\mathbf{r},t)$ and $\mathbf{A}(\mathbf{r},t)$ are particle-particle interactions of the system. Analogous to this system, let us consider a second system with potentials $v'(\mathbf{r},t)$ and $\mathbf{A}'(\mathbf{r},t)$:

$$\hat{H}'(t) = \sum_{j=1}^{N}\left\{\frac{1}{2}\left[\frac{\nabla_j}{i} + \mathbf{A}'(\mathbf{r}_j,t)\right]^2 + v'(\mathbf{r}_j,t)\right\} + \frac{1}{2}\sum_{i,j\neq i}^{N} w'(\mathbf{r}_i - \mathbf{r}_j), \tag{2.59}$$

Considering a Taylor expansion of $\mathbf{A}'$, we can prove the system from eqn. 2.62 produces equal time-dependent particle and current densities $n(\mathbf{r},t)$ and $\mathbf{j}(\mathbf{r},t)$ as the system from eqn. 2.58. In this way, we can consider up-to-gauge transformations to uniquely determine the potentials $v'(\mathbf{r},t)$ and $\mathbf{A}'(\mathbf{r},t)$. Considering two possibilities, the theorem of TDCDFT states:

- If both systems are equal ($\Psi(0) = \Psi'(0)$). There is a one-to-one mapping between the pair of scalar and vector potential and the particle and current densities:

$$\{v(\mathbf{r},t), \mathbf{A}(\mathbf{r},t)\} \Longleftrightarrow \{n(\mathbf{r},t), \mathbf{j}(\mathbf{r},t)\}, \tag{2.60}$$

- If w' is set to vanish in the second system, the particle and current densities of an interacting system can be obtained in a noninteracting system by the Hamiltonian

$$\hat{H}_s(t) = \sum_{j=1}^{N} \left\{ \frac{1}{2} \left[\frac{\nabla_j}{i} + \mathbf{A}_s(\mathbf{r}_j,t) \right]^2 + v_s(\mathbf{r}_j,t) \right\}. \tag{2.61}$$

Then, the TDKS equation in the TDCDFT framework:

$$i\frac{\partial}{\partial t}\phi_j(\mathbf{r},t) = \left(\frac{1}{2} \left[\frac{\nabla}{i} + \mathbf{A}_s(\mathbf{r},t) \right]^2 + v_s(\mathbf{r},t) \right) \phi_j(\mathbf{r},t) \tag{2.62}$$

2.3.5 Linear response theory in TDDFT

One of the approaches to solve the TD Khon-Sham equations 2.55 is within the framework of real-time time-dependent DFT in the adiabatic approximation[46]. A trendy approach to consider Casida first derived the linear-response TDDFT[56], in which the time-dependent density can be defined as:

$$n(\mathbf{r},t) = 2\sum_{i}^{occ} |\phi_i(\mathbf{r},t)|^2, \tag{2.63}$$

where a spin-unpolarized system is being considered. The coupling of a TD system with an external electric field can be defined in the dipole approximation:

$$\mathbf{E}(\mathbf{t}) = \hat{\mathbf{n}}\kappa\delta(t), \tag{2.64}$$

where $\hat{\mathbf{n}}$ defines the polarization direction, κ is the kick strength, and the $\delta(t)$ is the Dirac delta function. Then, the effect of perturbing the system,

$$\phi_i(\mathbf{r},0^+) = e^{i\kappa\hat{\mathbf{n}}\cdot\mathbf{r}}\phi_i(\mathbf{r},0^-), \tag{2.65}$$

then, the wavefunctions of the system are propagated by a finite time, and the induced dipole moment of the system is:

$$\mathbf{d}(t) = -\int d^3r\mathbf{r}[n(\mathbf{r},t) - n_g(\mathbf{r})] \tag{2.66}$$

The absorption spectrum can be calculated by taking the imaginary part of the Fourier transform the dipole moment $\mathbf{d}(t)$[57] to obtain the dynamic polarizability $\alpha(w)$:

$$\alpha(w) = \frac{1}{\kappa}\int dte^{iwt}[d(t) - d(0)]. \tag{2.67}$$

To calculate the absorption spectrum, the imaginary part of this function is taken:

$$S(w) = \frac{2w}{\pi}\Im(\alpha(w)) \tag{2.68}$$

Applying the "f-sum rule", the dipole oscillator strength distribution function can provide a direct connection with the number of electrons N, given by the integral:

$$N = \int dwS(w) \tag{2.69}$$

which is the integral form of the Thomas-Reiche-Khun (TRK) sum rule[58] for the interaction of light with solids. This described approach will later be used to analyze absorption spectra. To probe the linear response, the strength of the excitation should be low, and the propagation should run for a long interval.

2.3.6 Laser Dynamics

Let us consider the time-dependent KS equation in the velocity-gauge formalism:

$$i\partial_t\phi_j(\mathbf{r},t) = \left(\frac{1}{2}\left(-i\nabla + \frac{\mathbf{A}(t)}{c}\right)^2 - \sum_i \frac{Z_i}{|\mathbf{R}_i - \mathbf{r}|} + \int d^3r' \frac{n(\mathbf{r}',t)}{|\mathbf{r}-\mathbf{r}'|} + v_{xc}[n(\mathbf{r},t)]\right)\phi_j(\mathbf{r},t), \tag{2.70}$$

which has been an extremely successful formulation when considering molecules[59] and non-periodic systems; however, several extensions have also been made to consider solids[60,61]. Then, in order to calculate the response of the material to an ultrafast laser pulse, one should consider an electric field of the form:

$$\mathbf{E}(t) = -\frac{1}{c}\frac{d\mathbf{A}(t)}{dt} \tag{2.71}$$

Having the time-dependent KS orbitals, one can describe the macroscopic current:

$$\mathbf{J}(t) = \int_\eta d^3r\frac{1}{2}\sum_j\left[\phi_j^*(\mathbf{r},t)\left(-i\nabla + \frac{\mathbf{A}(t)}{c}\right)\phi_j(\mathbf{r},t) + c.c.\right], \tag{2.72}$$

where the integration is considering the unit cell volume η. In order to probe high-harmonic generation, the harmonic emission spectrum can be expressed as:

$$H(w) = |\int dt\partial_t\mathbf{J}(t)e^{-iwt}|^2 \tag{2.73}$$

A last calculation regarding the laser-induced dynamics, where the number of excited electrons at a certain time t, can be defined as:

$$N_{ex}(t) = N_{total} - \sum_{n,n',\mathbf{k}} P_{n',\mathbf{k}}(t) |\langle \phi_{n\mathbf{k}}(t=0) | \phi_{n'\mathbf{k}}(t) \rangle|^2, \tag{2.74}$$

where $P_{n',\mathbf{k}}(t)$ is the population of the "n′-th" state at **k** and time t.

2.4 The Vienna *ab initio* Simulation Package (VASP)

Simulations *ab initio* have become an essential aspect of material science areas for predicting and reproducing physical properties (atomic and electronic structure, optical, magnetic, and mechanical properties) of many types of systems. This section will introduce some vital computational details to carry on several simulations in this work. The *ab initio* simulation package (VASP) is a plane-wave code that uses the projector-augmented-wave approach (PAW)[62] to describe electron-electron interactions accurately. Since its development by Georg Kreese and his coworkers[63–65], VASP has acquired all the DFT levels, including Green's functions and many-body perturbation theory.

In order to accurately predict the valence orbitals, charge densities, and potentials, the VASP code uses plane-wave methods because it offers many advantages: (i) one can always control the convergence of the basis set[66]. (ii) To obtain the forces and stress on the material, one can rely on the Hellman-Feynman theorem to calculate the expectation value of the Hamiltonian[67].

To treat the bound inert core electrons, one can use pseudopotentials that consider local-basis set methods in exchange for the calculation's computational effort. To make calculations on solid systems possible, VASP uses PAW pseudopotentials. However, this is sometimes a disadvantage because of the need to include nonlinear corrections to treat valence-core interactions[68]. However, Kreese and Joubert's adapted and implemented correction[65] does not require these nonlinearity core-electron considerations because of the reached accuracy of the all-electron density.

2.5 The Octopus Code

All the RT-TDDFT calculations in this work were performed with the real-space grid code Octopus[69–72]. The study of nonlinear phenomena in solids has been prevalent since the advent of femtosecond laser pulses which can yield information about the electronic states of a system within these ultrafast-timescales that are relevant for several technological applications[73]. Solving the time-dependent KS equations can open the door to these processes in the linear and nonlinear-regime. Octopus is a pseudopotential real-space package to simulate electron-ion dynamics of systems under the perturbation of time-dependent electromagnetic fields. The represented quantities in the code are in a uniform grid in real space. One can use a simulated region with the shape of a sphere, a cylinder, or a parallelepiped. This work used the latter case considering different spacings in each orbital direction. However, a few disadvantages exist of using a real-space implementation, i.e., a calculated energy lower than the actual energy[74].

2.6 Methylammonium Lead Triiodide Perovskites

Perovskites are usually expressed with the formula ABX_3 in which a high symmetric cubic structure (α phase) can be maintained with a tolerance factor $t \rightarrow 1$, where $t = (R_A + R_X)/(\sqrt{2}(R_B + R_X))$, and R_X are the ionic radii of the corresponding ions. A value of $t < 1$ can lead to the formation of tetragonal or orthorhombic structures. At low temperatures, the fixed alignment of the $CH_3NH_3{}^+$ molecule causes this structure to be the most stable one, with low variation of the lattice constants and a more straightforward determination of the location of the $CH_3NH_3{}^+$ cations throughout experiments[75].

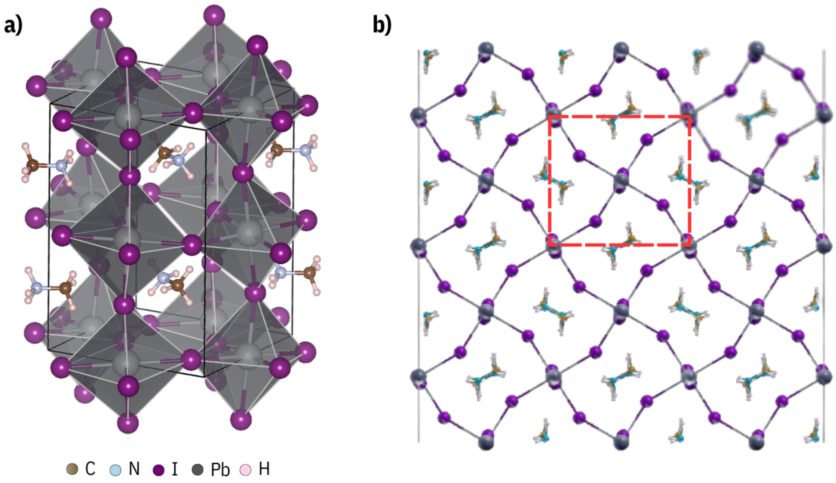

FIGURE 2.1: Atomic structure of the orthorhombic $CH_3NH_3PbI_3$ perovskite crystals. (a) The orthorhombic phase (space group *Pnma*) with optimized lattice parameters (experimental values in parentheses[76]): $a = 9.21$ (8.86) Å, $b = 8.86$ (8.58) Å, $c = 13.15$ (12.66) Å. (b) A side view of the δ phase of the $CH_3NH_3PbI_3$ perovskite.

This semiconductor material exhibits a direct transition at the R point or the Γ for the cubic and tetragonal structures in the Brillouin zone, respectively. An assignment of two prominent peaks is usually attributed to this structure: one narrow absorption peak near 1.64 eV and a second broad peak that comes from different transitions appearing within the range of 2.5 and 3.4 eV for an experimental absorption spectrum of a single crystal at 4 K[77]. Several already reported characteristics in DFT-calculated optical properties and experimental results can be made: (i) Usual range for the appearance of the prominent absorption peak is for values between 2.5 and 3.5 eV. (ii) High anisotropic behavior in the dielectric function of the tetragonal and orthorhombic phases, and (iii) the discrepancies of the dielectric function behavior between DFT calculations and experiments are evident. The main focus of this work is the orthorhombic phase of this material (the *Pnma* group), the analysis of the absorption spectrum of this material, and the ultrafast charge-carrier dynamics under the influence of incident pulses at different intensities.

Chapter 3

Methodology

The following chapter is devoted to introducing the two principal methodologies used in this work: the calculations using VASP with all-electron projected augmented wave (PAW) method[65,78], to describe structural and electronic properties of the material, and the calculations using the Octopus code under the framework of RT-TDDFT to induce the charge-carrier dynamics of the material under laser pulses at different intensities. When doing these simulations, one must always ensure that all the parameters the code uses converge in terms of the overall energy. This ensures that the computed properties are resolved consistently. In VASP, one must always look for cutoff energy and k-point mesh convergence. In Octopus, one should look for the spacing and k-point mesh convergence. Electron-ion interactions were described using ultrasoft pseudopotentials with a kinetic energy of 698.2 eV. Then, the procedure follows the variation of the cell parameters to ensure convergence of the cell volume and the total energies of the unit cell. Having all these values optimized, one can analyze the obtained electronic structure. During the simulations, valence states included Pb 6s, 6p, and 5d states, I 5s and 5p states, N 2s and 2p states, C 2s and 2p states, and the H 1s state. The $MAPbI_3$ perovskite structure is represented in a supercell containing 48 atoms (see fig. 2.1).

3.1 Optimization of parameters

3.1.1 VASP

The orthorhombic structure of the $MAPbI_3$ structure can be retrieved from numerous databases. The lattice parameters' values are usually very close to the experimental values[75,79]. The super cell with 48 atoms of this perovskite is shown in (see fig. 3.1), which was obtained from XCrySDen[80].

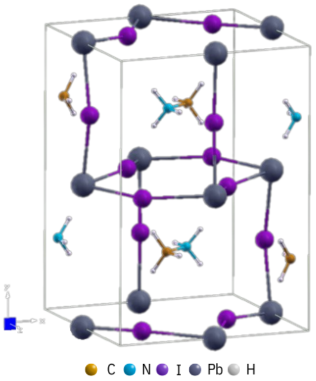

FIGURE 3.1: Crystal structure of the orthorhombic phase (space group *Pnma*) $CH_3NH_3PbI_3$ perovskite crystal used as an initial input for the VASP calculations.

As a starting point, we must ensure convergence of the cutoff energy of the system to ensure that the number of plane waves is enough to resolve the properties of the system. It can be seen in figure 3.2 that the energy of the system starts to converge from within an energy window of 1 meV/atom. Then, an appropriate energy cutoff for this system $E_{cut} = 850$ eV.

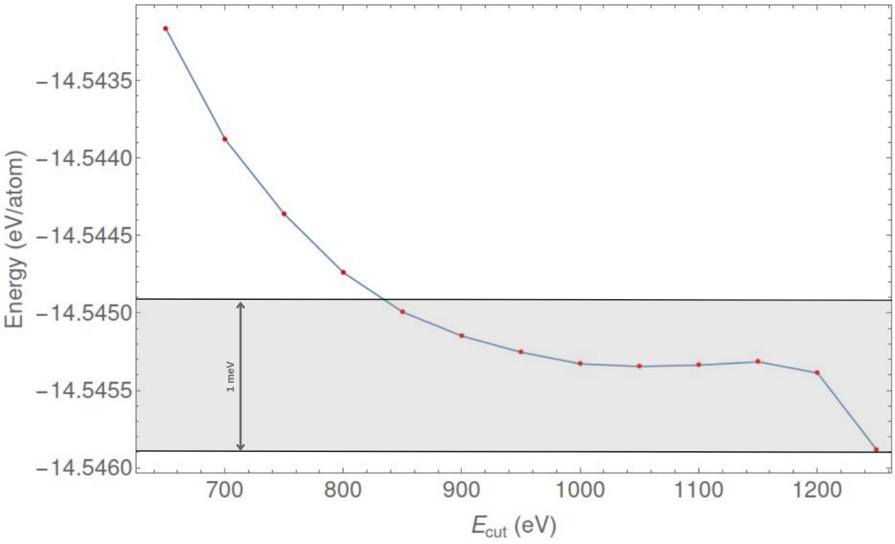

FIGURE 3.2: Convergence of the total energy with respect to the cutoff energy of the bulk structure in which a 1 mev/atom is achieved for a $E_{cut} = 850$ eV.

Another parameter that requires convergence is the number of $k-$points within the Monkhorst-Pack method implemented in the VASP code[81]. Within a convergence window of 1 meV/atom, the system reaches convergence for a $4 \times 3 \times 4$ k-points mesh which is equivalent to a separation $\Delta k = 0.028$ $\mathring{A}^{-1}$ and a total energy of 850 eV.

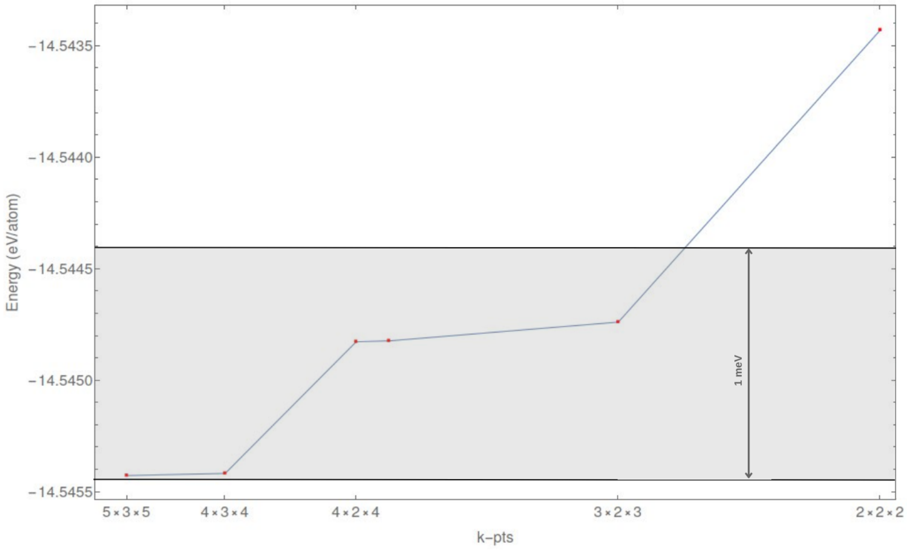

FIGURE 3.3: Energy convergence with respect to the k-poins mesh. The gray area represents the 1 meV/atom convergence range criteria. A $3 \times 2 \times 3$ k-mesh already starts to reach convergence.

Structural relaxation

This sets up the method to start calculations on this material. Thought out the work done in VASP, the functionals used were the r²SCAN+rVV10 functional[82], and the hybrid Heyd-Scuseria-Ernzerhof (HSE06) functional[30]. The objective now is to reach relaxation of the system's spatial configuration and find the optimal lattice parameters for the proposed unit cell. The equation of state to consider the direct dependence of the total energy of the system and the volume V, optimal volume V_0, the bulk modulus B', and the bulk modulus pressure derivative B_0' is the Birch-Murnaghan equation of state:

$$E(V) = E_0 + \frac{9V_0B_0}{16}\left\{\left[\left(\frac{V_0}{V}\right)^{\frac{2}{3}} - 1\right]^3 B_0' + \left[6 - 4\left(\frac{V_0}{V}\right)^{\frac{2}{3}}\right]\right\}. \tag{3.1}$$

In this framework, the following equation can be proposed to enable the fitting of our computed volumes:

$$E(V) = k_1 + k_2V^{-2/3} + k_3V^{-4/3} + k_4V^{-2} \tag{3.2}$$

where, for this case, the values were $k_1 = -6643.12$, $k_2 = 6.05 \times 10^9$, $k_3 = -1.80 \times 10^8$, and $k_4 = 1.79 \times 10^6$. The bulk modulus can be defined as:

$$B_0 = \left[V\frac{\partial^2}{\partial V^2}E(V)\right]_{V\to V_0} \tag{3.3}$$

Finally, B_0' is computed in the following way:

$$B_0' = \frac{\partial B_0}{\partial P}|_{V\to V_0} = -\frac{V}{B_0}\frac{\partial}{\partial V}\left[V\frac{\partial^2}{\partial V^2}E(V)\right]_{V\to V_0} \tag{3.4}$$

For a range of volumes, the computed optimal fitted volume is $V_0 = 995.3518\mathring{A}^3$ with a total energy of -700.19792 eV (see fig. 3.4), and a summary of the crystallographic data is compared with experimental data (see table 3.1). The computed values for the bulk modulus $B_0 = 21.1$ GPa , and the bulk modulus pressure derivative $B_0' = -8.2$. It has to be mentioned that this optimization motivated the analysis of the density of states calculated with the HSE06 functional with the lattice parameters from the r²SCAN calculations.

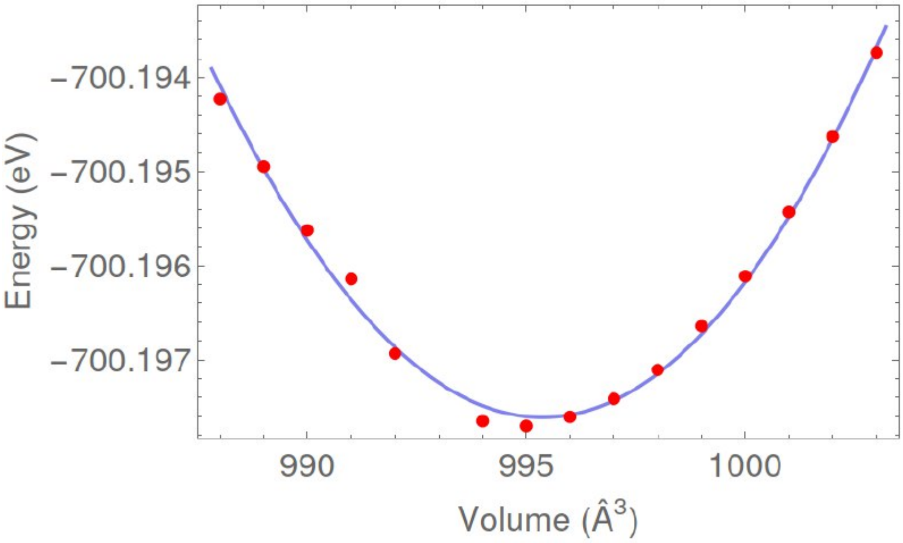

FIGURE 3.4: Computed 3^{th} order Birch-Murnagham EOS using r²SCAN+*r*VV10.

TABLE 3.1: Computed r²SCAN+*r*VV10 crystallographic data for the optimal unit cell of the $CH_3NH_3PbI_3$ perovskite and experimental data.

Property	r²SCAN+*r*VV10	Experimental[75,83]
Space Group	*Pnma*	Pnma (no. 62)
a (Å)	9.21	8.86, 8.83
b (Å)	13.15	12.66, 12.58
c (Å)	8.86	8.58, 8.55
V (Å^3)	995.35	962.54, 951.01

3.1.2 Octopus

Spacing and k-points

Several methodologies and optimization procedures will be introduced to ensure a proper workflow toward the dynamical calculations performed with the real-space grid code Octopus. We worked in the adiabatic local density approximation (ALDA) to approximate the exchange-correlation functional[31], and the Hartwigsen-Goedecker-Hutter (HGH)[84] LDA pseudopotentials as an approximation of the core electrons. In Octopus, we specify every system characteristic in only one input. Therefore, we will specify each block that determines critical parameters for our calculations:

- **Calculation mode:** This specifies the run mode. In the case of a ground state calculation, the run mode is specified to be "gs". However, several other modes, such as "unocc" and the "td" modes, will be used through our calculations.
- **Coordinates:** This block presents the atomic species and positions in our structure. This variable is defined as a block of variables. The strategy used in this work was to define an alternate *.xyz* file within this block.
- **Spacing:** It defines the spacing between points in a real-space cubic mesh.
- **KPointsGrid:** This variable defines the k-point grid used in the calculation. One can also define the reciprocal-space mesh by explicitly setting the position of each k-point.

Now, determining an appropriate value for the spacing of two points in each Cartesian direction is a key parameter for the convergence study. We display the $MAPbI_3$ structure results in fig. 3.5.

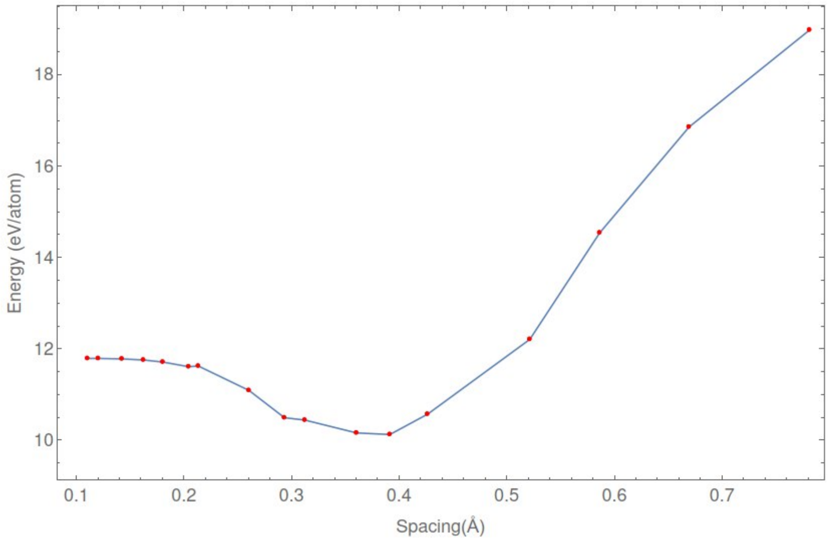

FIGURE 3.5: Energy convergence of the $MAPbI_3$ perovskite with respect to the spacing. The system reaches a converged value starting from 0.18Å.

In order to sample the Brillouin zone, one must always have to ensure the use of an appropriate k-mesh. Similar to the previous procedure in VASP, the system converges when we use a $5 \times 3 \times 5$ set of k-points.

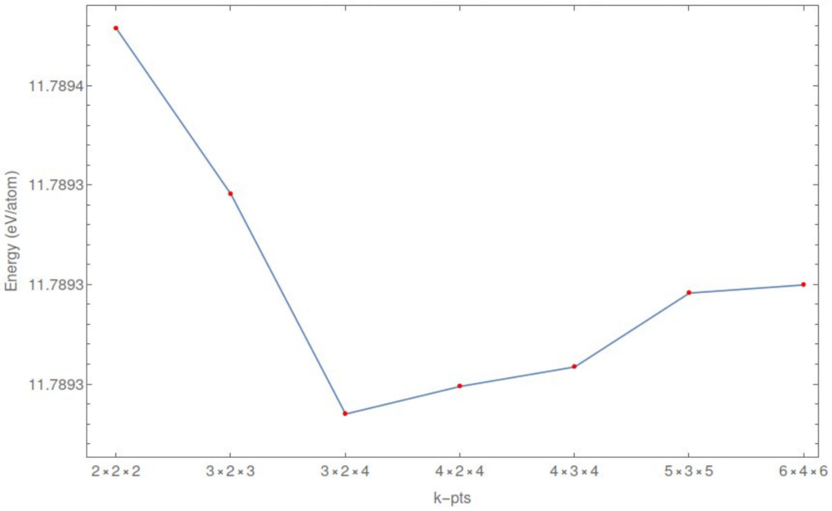

FIGURE 3.6: Energy convergence of the $MAPbI_3$ perovskite with respect to the k-points. The system reaches a converged value starting from the $5 \times 3 \times 5$ k-points mesh.

TD calculations

To perform a time-dependent propagation, the "td" calculation has to be defined. Another set of essential values are the "TDTimeStep" and the "TDMaxSteps" parameters. Considering the propagation length T, and Δt length of the time step, the "TDMaxSteps" variable can be defined as a number of iterations $T/\Delta t$. Without a perturbation, the system's energy shall remain unchanged. Our TD calculations begin by calculating the absorption spectrum in different directions using the delta kick approach[48]. Then, the objective is to calculate linear properties of the $MAPbI_3$ perovskite by following the system's evolution under the influence of a laser treated in the dipole approximation. Then, the harmonic emission spectrum can be calculated from the acceleration of the dipole moment:

$$H(w) \propto \left| \int dte^{iwt} \frac{d^2}{dt^2} d(t) \right|^2 \tag{3.5}$$

As a result of the propagation, charge density is absorbed at the boundaries of the simulated region, either by an imaginary potential or a mask function. In the case of the imaginary absorbing potential, a term should be added to the Khon-Sham potential:

$$Veff(r,t) = V_{KS}(r,t) - iV_{abs}(r), \tag{3.6}$$

where this extra term rises from zero in the inner regions up to the limits of the simulated region.

Chapter 4

Results and Discussion

The results in this section will involve the calculations regarding electronic properties and key descriptors of the dynamical behavior of the charge carriers in the system.

4.1 Electronic structure analysis

4.1.1 Density of states

This section will report several results obtained from Octopus and VASP to compare the computed properties and their behaviors concerning each functional. Once the structural relaxation of the system is acquired, the objective is to study the electronic properties of $MAPbI_3$. We plotted the total and the projected density of states (DOS and PDOS) of the structures calculated with the HSE06 (see fig. 4.1 (a)) functional and the r²SCAN+*r*VV10 (see fig. 4.1 (b)), where only minor differences between these calculations can be resembled. A closer look at the partial density of the valence band maximum (VBM) can show a more significant contribution from Pb 6*s* and I 5*p* states and a more significant contribution to the conduction band minimum (CBM) coming from a Pb state. The organic $CH_3NH_3{}^+$ organic molecule is far from the Fermi energy level region. Since C, N, and H bands locate in another region of energy from -4.8 eV; no covalent interaction can exist between the Pb-I structure and the organic cation.

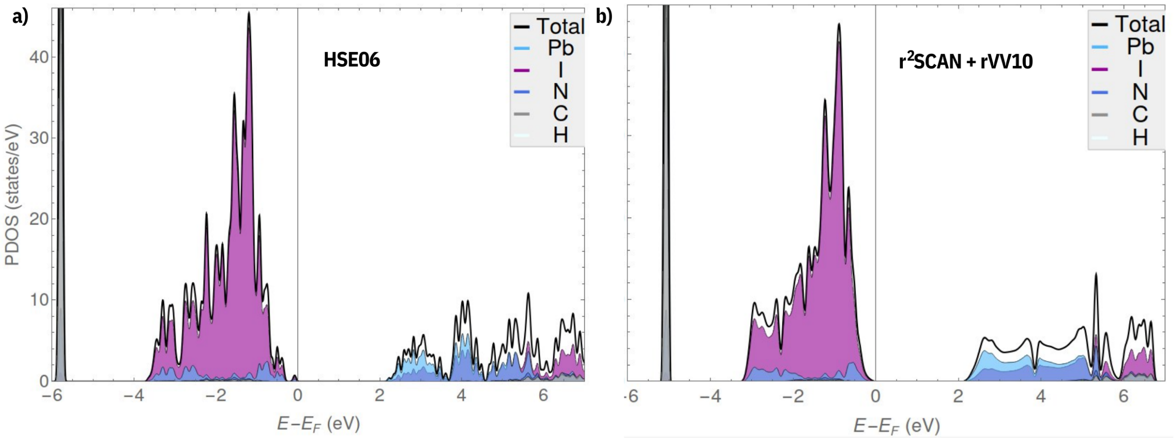

FIGURE 4.1: Total density of states and partial density of states (PDOS) of an orthorhombic $CH_3NH_3PbI_3$ structure using the HSE06 functional (a) and the r²SCAN+*r*VV10 functional (b).

4.1.2 Band structure

The $CH_3NH_3PbI_3$ perovskite is a semiconductor material with a direct band gap at the Γ point (tetragonal and orthorhombic structure)[75,85,86] or the R point (cubic structure)[75,86] in the Brillouin zone. We report here the band structure of the $MAPbI_3$ perovskite calculated within the LDA approximation (E_{gap} = 1.47 eV), and the r²SCAN+*r*VV10 functional (E_{gap} = 2.10 eV). It has to be mentioned that to acquire an E_{gap} very close to the absorption edge in the 1.6 eV region; one must account for spin-orbit coupling (SOC). Even though the SOC effect is not included, we can still obtain a good description of the system's electronic structure and band character.

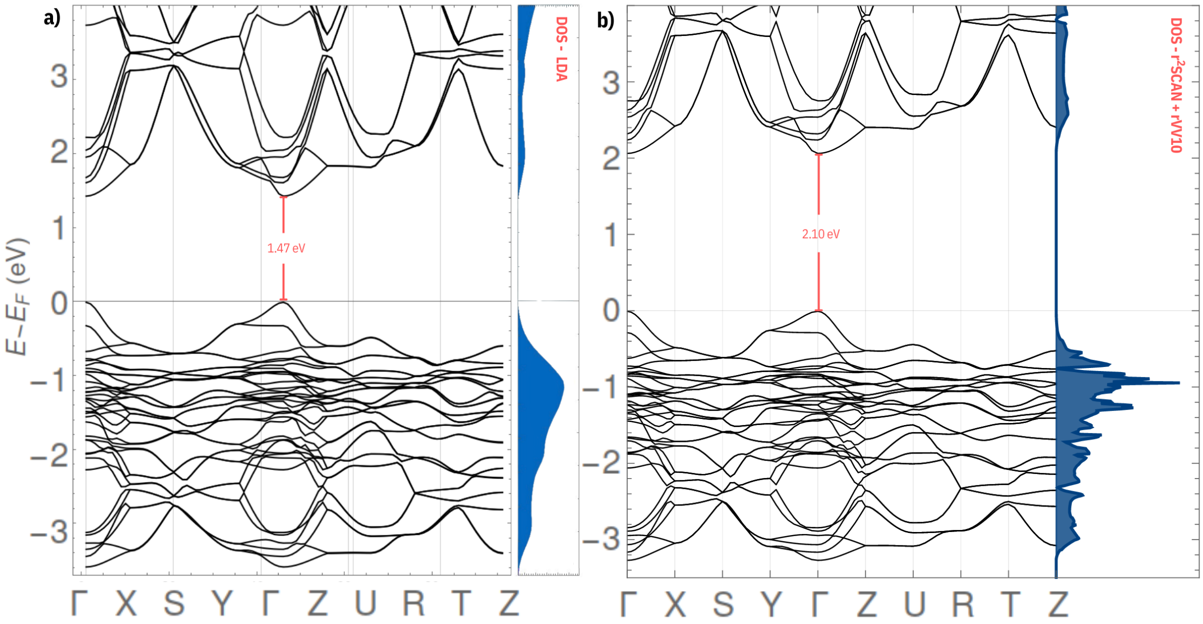

FIGURE 4.2: Calculated band structure of orthorhombic supercell of the $CH_3NH_3PbI_3$ perovskite along the high-symmetry lines in the first Brillouin zone using the LDA approximation (a) and the r²SCAN+*r*VV10 functional (b).

The fact that the bands are broad near the VBM indicates that the states are non-local, and it explains why this material exhibits long-range carrier-diffusion lengths[87]. Conversely, these fluctuations within the CBM indicate faster transport of photoelectrons from experimental studies[88]. From the results of the density of states and the band structure, it can already be concluded that the electronic states corresponding to the molecule are highly localized in space, preventing substantial interaction with the inorganic component of the perovskite. The analysis done for the DOS and band structure already tells us that to photoexcite electrons, a perturbation with sufficient energy will photoexcite I 5*p* electrons to Pb 6*p* empty states. However, more precise information regarding the type of excitation and the charge carriers' behavior is necessary, especially in real-time.

4.2 Linear Absorption Spectrum

Numerous reported results on the optical of $MAPbI_3$ can be found[89–91], but most of these resources present discrepancies between their obtained optical data. The main reason for this discrepancy is the influence of surface roughening and structural non-uniformity in the growth direction. We report here the absorption spectrum of our material within the framework of RT-ALDA (see fig. 4.3(a)). It can be noticed that the system exhibits a high peak in the high-energy region at 3.14 eV, which is consistent with several reported optical transitions reported in experiments[89], which usually report two high energy peaks at $E_1 = 2.53 \pm 0.01$ eV and $E_2 = 3.24 \pm 0.01$ eV. We also report the presence of E_0=1.47 eV, E_1=2.54 eV, and E_2=3.19 eV, these values show excellent agreement with the experimental results, and all the fine absorption features observed experimentally in these perovskites are reproduced reasonably well. Our reported peak at 3.1 eV has been reported in several experiments to be caused by excitonic transition[92].

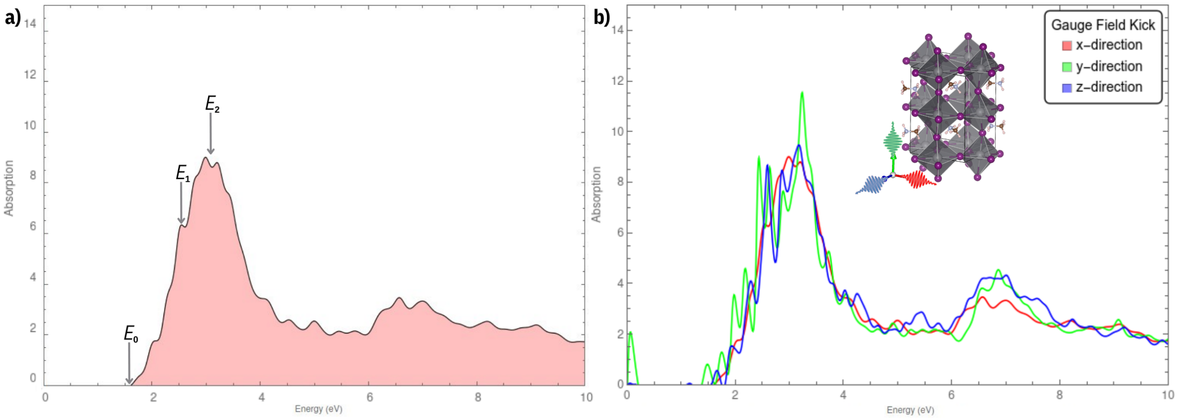

FIGURE 4.3: Absorption spectra of the $MAPbI_3$ perovskite structure for $\hat{\mathbf{x}}$ polarization direction (a), where we report two high energy peaks at E_1 and E_2. Absorption spectra (b) assuming different polarization directions along the x, y, and z axes.

The next objective in our calculations was to test the dependency of the obtained absorption spectrum with the direction of the perturbation. The results in fig 4.3(b) show that the variation of the polarization direction produces minor variations in the main peaks. A summary of the main peaks according to the polarization direction change of the absorption spectrum can be seen in table 4.1.

$\hat{\mathbf{n}}$	E_0 (eV)	E_1 (eV)	E_2 (eV)
$\hat{\mathbf{x}}$-dir	1.59	2.54	3.19
$\hat{\mathbf{y}}$-dir	1.38	2.42	3.23
$\hat{\mathbf{z}}$-dir	1.54	2.58	3.16

TABLE 4.1: Summary of the main peaks appearing in the absorption spectrum of $MAPbI_3$ when varying the polarization direction of the Gauge field kick.

4.3 Ultrafast charge-carrier dynamics

4.3.1 Induced electric current density

In this section, we will investigate the electron dynamics of the $MAPbI_3$ perovskite within a time window of 20 fs after the laser is switched off. We report the electric current density $J(t)$ (eqn 2.72) to monitor the response of the system to the time-dependent perturbation of varying peak intensities. It can be seen in fig. 4.4 that the current starts to build up when the laser is turned on, exhibiting an oscillatory behavior similar to the applied field. Consider a 20 fs time window after the perturbation is switched off. A residual weaker, almost constant behavior of the density is a signature of the remaining coherence between ground-and-excited-states. Considering that no dissipation channels exist, the system's response will not decay over time. On the other side, under the action of stronger pulses (see fig. 4.4(d)), the response of the system does not show a periodic pattern anymore. This behavior of the system is associated with a nonlinear response. Baikie, T.; Fang, Y.; Kadro, J. M.; Schreyer, M.; Wei, F.; Mhaisalkar, S. G.; Graetzel, M.; White, T. J. Journal of Materials Chemistry A 2013, 1, 5628–5641.Under the weaker pulse, the system reacts to create a coherent oscillation from energetically similar states.

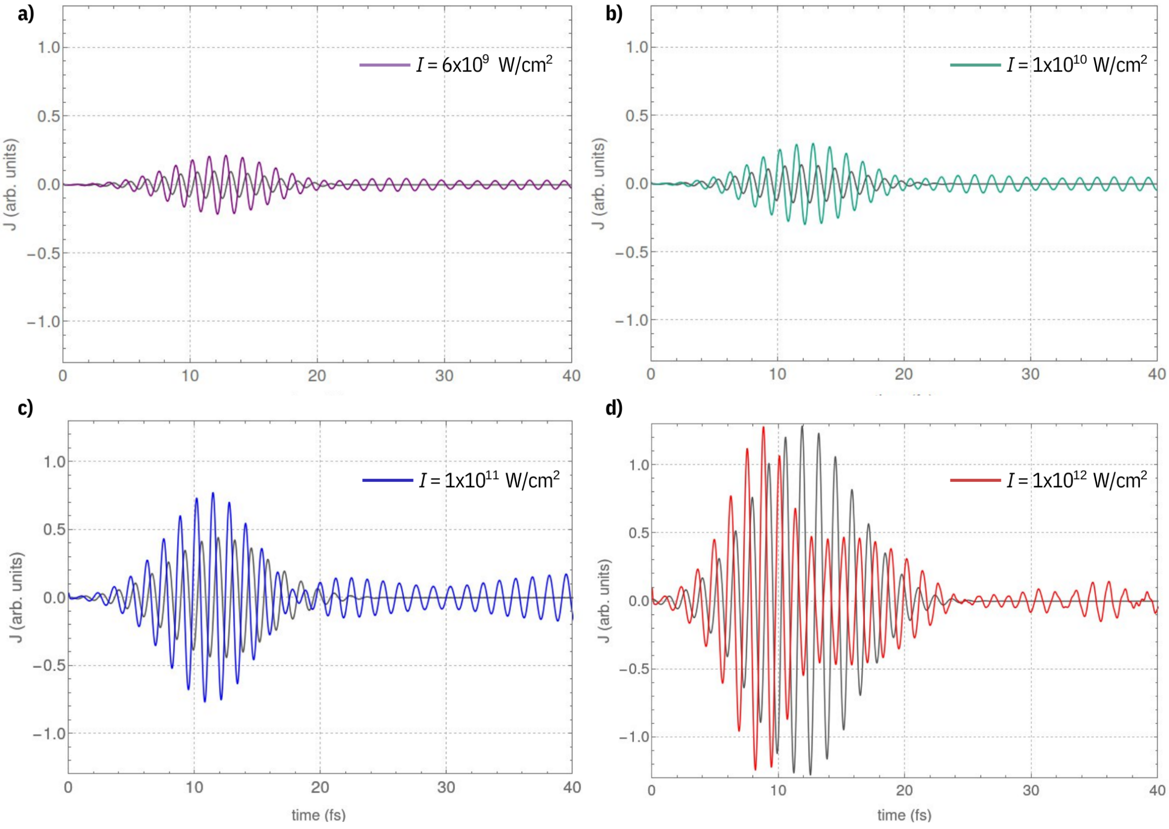

FIGURE 4.4: Time evolution of the induced electric current density, $J(t)$, at varying intensities of the laser pulse, represented in black in the background: (a) $I = 6 \times 10^9\ W/cm^2$, (b) $I = 1 \times 10^{10}\ W/cm^2$, (c) $I = 1 \times 10^{11}\ W/cm^2$, and (d) $I = 1 \times 10^{12}\ W/cm^2$.

To confirm the nonlinear nature response of the system, we report here the results of calculating the harmonic spectrum $H(\omega)$ (eqn 3.5). The spectrum shows that the appearance of extra carrier frequencies (ω_1, and ω_2) only occurs at high intensities. Conversely, weaker pulses only reveal the fundamental harmonic corresponding to the natural carrier frequency, ω_0 = 3,12 eV. When a $I = 1 \times 10^{12}$ W/cm^2, maxima are present at ω_1 = 9.21 eV, and at ω_2 =15.70 eV. Multiple side peaks near the harmonics are a signature of multiphoton absorption. This confirms the nonlinear regime of the interaction.

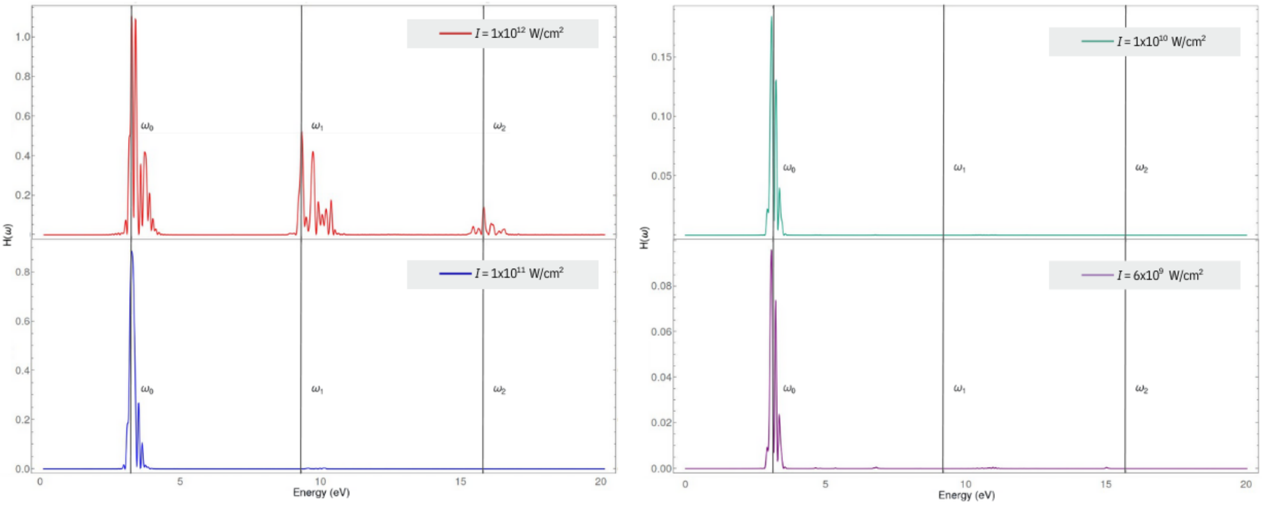

FIGURE 4.5: High-harmonic spectrum, $H(\omega)$, for the MAPbI$_3$ perovskite generated by pulses of increasing intensities. We displayed the fundamental carrier frequency (ω_0) and its overtones (ω_1 and ω_2).

4.3.2 Excitation energy

Finally, we proceed to monitor the excitation energy, $\Delta E_{ex}(t) = E(t) - E(t = 0)$, calculated as the difference between the electronic energy at a certain time $t > 0$ and in the ground state[93,94]. We report these results in fig. A.1 following the corresponding color code, and the evolution can be seen in fig. A.1(b) displayed up to 40 fs. The relation between the excitation energy and the laser intensity suggests linear response for $I = 1 \times 10^{11}$ W/cm^2, where $\Delta E_{ex}(t = 40fs) = 0.09$ eV/atom; for $I = 1 \times 10^{10}$ W/cm^2, where the $\Delta E_{ex}(t = 40fs) = 0.007$ eV/atom; and for $I = 6 \times 10^9$ W/cm^2, where the $\Delta E_{ex}(t = 40fs) = 0.001$ eV/atom. The time evolution of the excitation energy difference (fig. A.1(b)) indicates that, after 20 fs, this quantity forms a plateau that does not change because of the absence of dissipation effects. This behavior has already been reported in the literature for insulators[95], semiconductors[96], graphite thin films[97], and dielectrics[98].

Then, we analyze the response of the perovskite by collecting information regarding the number of excited electrons within the 40 fs time window. The behavior is very similar to $\Delta E_{ex}(t)$, in which the value of this quantity increases steeply when the pulse is present and reaches a maximum of about 12 fs.

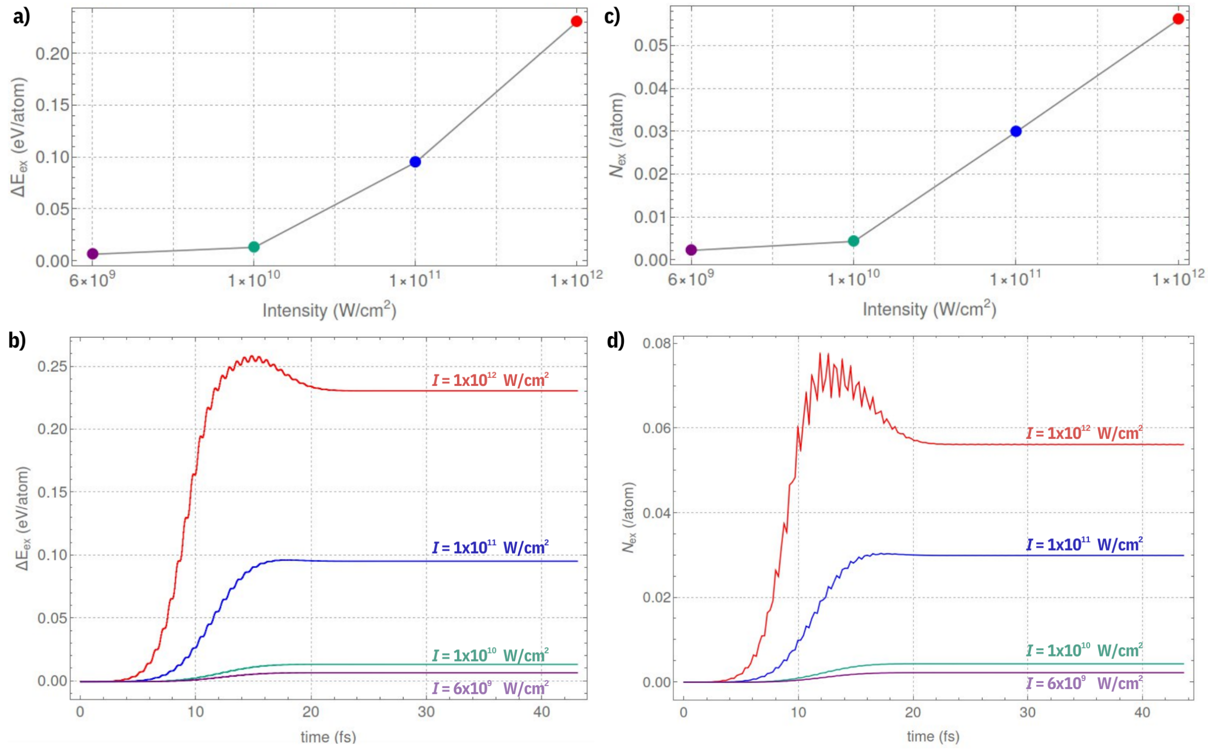

FIGURE 4.6: Excitation energy $\Delta E_{ex}(t) = E(t) - E(t = 0)$ as a function of the laser intensity (a) with t = 40 fs and (b) within the entire temporal range. Number of excited electrons, $N_{ex}(t)$ (c) with t=40 fs and (d) within the entire temporal range.

Chapter 5

Conclusions and future work

We have investigated several structural and electronic properties of the $CH_3NH_3PbI_3$ perovskite using density-functional theory with and without time dependency. The band gap and electronic localization description agree with previous simulations made on this perovskite. Furthermore, the reported results about the localization of atoms served as a basis for understanding several of the light-induced processes proposed later.

This work was able to report the absorption spectra of the system in the ALDA regime, where the predicted main peaks are very similar to the ones reported in the literature. These results show a small non-anisotropy dependence on the optical properties of the material. Within the framework of RT-TDDFT, we have investigated the laser-driven charge-carrier dynamics of the $CH_3NH_3PbI_3$ perovskite orthorhombic structure. Inducing a laser excitation of intensities 6 to 1000 GW/cm^2 in the system shows the intensity-dependence in the nonlinear behavior of the number of excited electrons and in the induced electric current density behavior at later times. Our main objective was to present calculations of several descriptors that can help us understand the physics of the ultrafast dynamical processes in this type of perovskites. Even though the TD calculations are based on the ALDA approach, we can capture the nature and some of the main properties of the system. This is confirmed by several of the electronic properties we calculated, where the band gap and band behavior prediction is very close to results obtained using even more robust approaches. The computational analysis of this semiconductor material's ultrafast and nonlinear optical responses can give insights into the carrier generation and dynamics of novel semiconductor materials in a femtosecond timescale. Further in-depth analysis of the charge transfer that occurs in the material during the time window of the simulations is essential to understand the effect of the perturbation in electron localization clearly.

Appendix A

Data analysis

A.1 Density of states

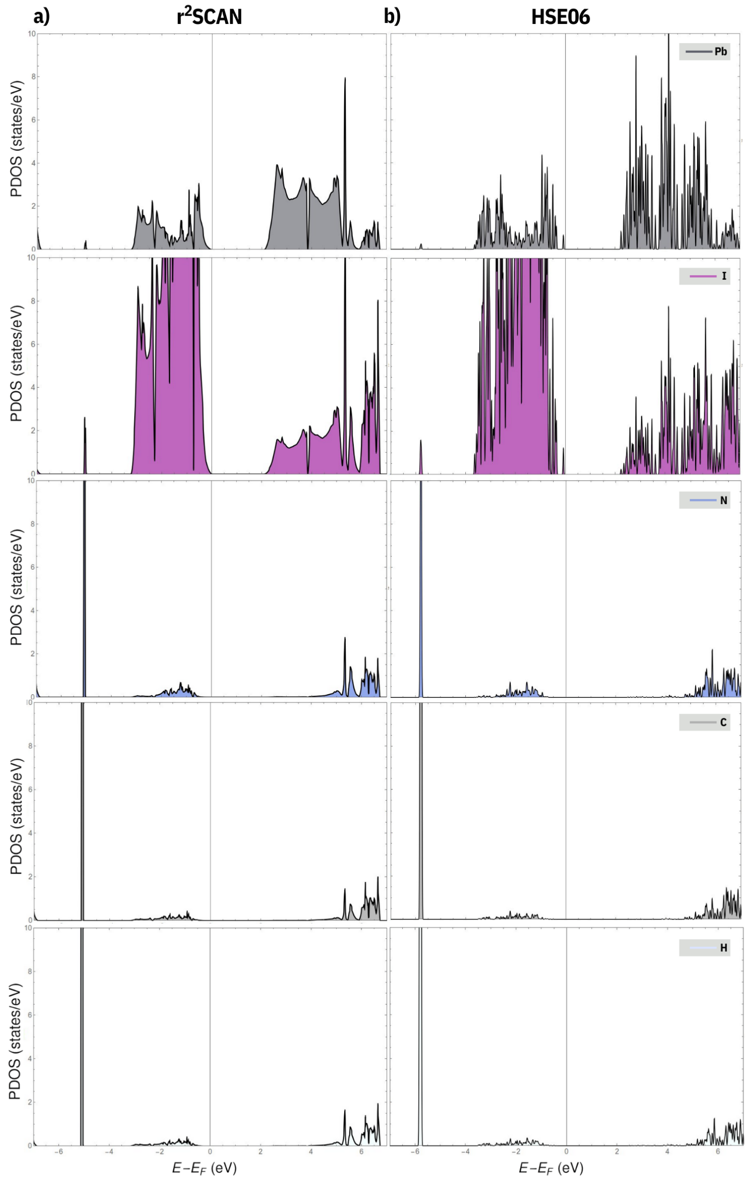

FIGURE A.1: Partial densoty of states of atoms in orthorhombic $CH_3NH_3PbI_3$ perovskite structures using the r²SCAN+*r*VV10 functional.

Bibliography

(1) Ponseca Jr, C. S.; Savenije, T. J.; Abdellah, M.; Zheng, K.; Yartsev, A.; Pascher, T.; Harlang, T.; Chabera, P.; Pullerits, T.; Stepanov, A., et al. *Journal of the American Chemical Society* **2014**, *136*, 5189–5192.

(2) Burschka, J.; Pellet, N.; Moon, S.-J.; Humphry-Baker, R.; Gao, P.; Nazeeruddin, M. K.; Grätzel, M. *Nature* **2013**, *499*, 316–319.

(3) Xing, G.; Mathews, N.; Sun, S.; Lim, S. S.; Lam, Y. M.; Grätzel, M.; Mhaisalkar, S.; Sum, T. C. *Science* **2013**, *342*, 344–347.

(4) Liu, M.; Johnston, M. B.; Snaith, H. J. *Nature* **2013**, *501*, 395–398.

(5) Bi, D.; Yang, L.; Boschloo, G.; Hagfeldt, A.; Johansson, E. M. *The journal of physical chemistry letters* **2013**, *4*, 1532–1536.

(6) Yang, W. S.; Noh, J. H.; Jeon, N. J.; Kim, Y. C.; Ryu, S.; Seo, J.; Seok, S. I. *Science* **2015**, *348*, 1234–1237.

(7) Kojima, A.; Teshima, K.; Shirai, Y.; Miyasaka, T. *Journal of the american chemical society* **2009**, *131*, 6050–6051.

(8) Chang, Y.; Park, C. H.; Matsuishi, K. *Journal-Korean Physical Society* **2004**, *44*, 889–893.

(9) Borriello, I.; Cantele, G.; Ninno, D. *Physical Review B* **2008**, *77*, 235214.

(10) Mourou, G.; Fisch, N.; Malkin, V.; Toroker, Z; Khazanov, E.; Sergeev, A.; Tajima, T; Le Garrec, B *Optics Communications* **2012**, *285*, 720–724.

(11) Tancogne-Dejean, N.; Mücke, O. D.; Kärtner, F. X.; Rubio, A. *Physical review letters* **2017**, *118*, 087403.

(12) Schrödinger, E. *Physical review* **1926**, *28*, 1049.

(13) Watson, D. K.; Dunn, M. *Physical review letters* **2010**, *105*, 020402.

(14) Conroy, H. *The Journal of Chemical Physics* **1964**, *41*, 1327–1331.

(15) Froese Fischer, C. *Journal of Computational Physics* **1973**, *13*, 502–521.

(16) Tiesinga, E.; Mohr, P. J.; Newell, D. B.; Taylor, B. N. *Journal of Physical and Chemical Reference Data* **2021**, *50*.

(17) Dobson, J. F.; Vignale, G.; Das, M. P. **2013**.

(18) Born, M.; Huang, K.; Lax, M *American Journal of Physics* **1955**, *23*, 474–474.

(19) Born, M; Oppenheimer, R **1927**.

(20) Slater, J. C. *Physical Review* **1930**, *35*, 210.

(21) James, R. W.; Waller, I; Hartree, D. R. *Proceedings of the Royal Society of London. Series A, Containing Papers of a Mathematical and Physical Character* **1928**, *118*, 334–350.

(22) Fock, V. *Zeitschrift für Physik* **1930**, *61*, 126–148.

(23) Szabo, A; Ostlund, N. *Modern Quantum Chemistry* **1996**.

(24) McWeeny, R; Sutcliffe, B.; Brink, G. *Physics Today* **1971**, *24*, 50–50.

(25) Hohenberg, P.; Kohn, W. *Physical review* **1964**, *136*, B864.

(26) Giustino, F., *Materials modelling using density functional theory: properties and predictions*; Oxford University Press: 2014.

(27) Perdew, J.; Schmidt, K *Proc. 577* **2001**, *1*.

(28) Perdew, J. P.; Zunger, A. *Physical Review B* **1981**, *23*, 5048.

(29) Furness, J. W.; Kaplan, A. D.; Ning, J.; Perdew, J. P.; Sun, J. *The journal of physical chemistry letters* **2020**, *11*, 8208–8215.

(30) Heyd, J.; Scuseria, G. E.; Ernzerhof, M. *The Journal of chemical physics* **2003**, *118*, 8207–8215.

(31) Perdew, J. P.; Zunger, A. *Physical Review B* **1981**, *23*, 5048.

(32) Ismail-Beigi, S.; Arias, T. A. *Physical review letters* **1999**, *82*, 2127.

(33) Herman, F.; Van Dyke, J. P.; Ortenburger, I. B. *Physical Review Letters* **1969**, *22*, 807.

(34) Perdew, J. P.; Ruzsinszky, A.; Csonka, G. I.; Vydrov, O. A.; Scuseria, G. E.; Constantin, L. A.; Zhou, X.; Burke, K. *Physical review letters* **2008**, *100*, 136406.

(35) Becke, A. D. *Physical review A* **1988**, *38*, 3098.

(36) Zhang, Y.; Yang, W. *Physical Review Letters* **1998**, *80*, 890.

(37) Santra, G.; Martin, J. M. *Molecules* **2021**, *27*, 141.

(38) Perdew, J. P.; Burke, K; Ernzerhof, M *Physical Review Letters* **1998**, *80*, 891.

(39) Swathilakshmi, S; Devi, R.; Sai Gautam, G. *Journal of Chemical Theory and Computation* **2023**.

(40) Sun, J.; Remsing, R. C.; Zhang, Y.; Sun, Z.; Ruzsinszky, A.; Peng, H.; Yang, Z.; Paul, A.; Waghmare, U.; Wu, X., et al. *Nature chemistry* **2016**, *8*, 831–836.

(41) Lane, C.; Zhang, Y.; Furness, J. W.; Markiewicz, R. S.; Barbiellini, B.; Sun, J.; Bansil, A. *Physical Review B* **2020**, *101*, 155110.

(42) Mardirossian, N.; Head-Gordon, M. *Molecular physics* **2017**, *115*, 2315–2372.

(43) Lee, C.; Yang, W.; Parr, R. G. *Physical review B* **1988**, *37*, 785.

(44) Paier, J.; Marsman, M.; Kresse, G. *The Journal of chemical physics* **2007**, *127*.

(45) Heyd, J.; Scuseria, G. E.; Ernzerhof, M. *The Journal of chemical physics* **2003**, *118*, 8207–8215.

(46) Runge, E.; Gross, E. K. *Physical review letters* **1984**, *52*, 997.

(47) Van Leeuwen, R. *Physical review letters* **1998**, *80*, 1280.

(48) Yabana, K.; Bertsch, G. *Physical Review B* **1996**, *54*, 4484.

(49) Olsen, J.; Jørgensen, P. In *Modern Electronic Structure Theory: Part II*; World Scientific: 1995, pp 857–990.

(50) Zangwill, A; Soven, P. *Physical Review A* **1980**, *21*, 1561.

(51) Ando, T. *Zeitschrift für Physik B Condensed Matter* **1977**, *26*, 263–272.

(52) Maitra, N. T.; Burke, K.; Woodward, C. *Physical review letters* **2002**, *89*, 023002.

(53) Maitra, N. T.; Souza, I.; Burke, K. *Physical Review B* **2003**, *68*, 045109.

(54) Botti, S.; Schindlmayr, A.; Del Sole, R.; Reining, L. *Reports on Progress in Physics* **2007**, *70*, 357.

(55) Vignale, G. *Physical Review B* **2004**, *70*, 201102.

(56) Casida, M. E. In *Recent Advances In Density Functional Methods: (Part I)*; World Scientific: 1995, pp 155–192.

(57) Sato, S.; Yabana, K; Shinohara, Y; Otobe, T; Bertsch, G. F. *Physical Review B* **2014**, *89*, 064304.

(58) Thomas, W. *Naturwissenschaften* **1925**, *13*, 627–627.

(59) Sottile, F.; Bruneval, F.; Marinopoulos, A.; Dash, L.; Botti, S.; Olevano, V.; Vast, N.; Rubio, A.; Reining, L. *International journal of quantum chemistry* **2005**, *102*, 684–701.

(60) Bertsch, G. F.; Iwata, J.-I.; Rubio, A.; Yabana, K. *Physical Review B* **2000**, *62*, 7998.

(61) Yabana, K.; Sugiyama, T; Shinohara, Y; Otobe, T; Bertsch, G. *Physical Review B* **2012**, *85*, 045134.

(62) Blöchl, P. E. *Physical review B* **1994**, *50*, 17953.

(63) Kresse, G.; Hafner, J. *Physical Review B* **1993**, *48*, 13115.

(64) Kresse, G; Furthmüller, J; Hafner, J. *Physical Review B* **1994**, *50*, 13181.

(65) Kresse, G.; Joubert, D. *Physical review b* **1999**, *59*, 1758.

(66) Paier, J.; Hirschl, R.; Marsman, M.; Kresse, G. *The Journal of chemical physics* **2005**, *122*.

(67) Feynman, R. P. *Physical review* **1939**, *56*, 340.

(68) Paier, J.; Hirschl, R.; Marsman, M.; Kresse, G. *The Journal of chemical physics* **2005**, *122*.

(69) Marques, M. A.; Castro, A.; Bertsch, G. F.; Rubio, A. *Computer Physics Communications* **2003**, *151*, 60–78.

(70) Castro, A.; Appel, H.; Oliveira, M.; Rozzi, C. A.; Andrade, X.; Lorenzen, F.; Marques, M *Phys. Stat. Sol. B* **2006**, *243*, 2465–2488.

(71) Andrade, X.; Strubbe, D.; De Giovannini, U.; Larsen, A. H.; Oliveira, M. J.; Alberdi-Rodriguez, J.; Varas, A.; Theophilou, I.; Helbig, N.; Verstraete, M. J., et al. *Physical Chemistry Chemical Physics* **2015**, *17*, 31371–31396.

(72) Tancogne-Dejean, N.; Oliveira, M. J.; Andrade, X.; Appel, H.; Borca, C. H.; Le Breton, G.; Buchholz, F.; Castro, A.; Corni, S.; Correa, A. A., et al. *The Journal of chemical physics* **2020**, *152*.

(73) Brabec, T.; Krausz, F. *Reviews of Modern Physics* **2000**, *72*, 545.

(74) Casida, M. E. *Journal of Molecular Structure: THEOCHEM* **2009**, *914*, 3–18.

(75) Baikie, T.; Fang, Y.; Kadro, J. M.; Schreyer, M.; Wei, F.; Mhaisalkar, S. G.; Graetzel, M.; White, T. J. *Journal of Materials Chemistry A* **2013**, *1*, 5628–5641.

(76) Poglitsch, A.; Weber, D. *The Journal of chemical physics* **1987**, *87*, 6373–6378.

(77) Ishihara, T. *Journal of luminescence* **1994**, *60*, 269–274.

(78) Kresse, G.; Furthmüller, J. *Physical review B* **1996**, *54*, 11169.

(79) Poglitsch, A.; Weber, D. *The Journal of chemical physics* **1987**, *87*, 6373–6378.

(80) Kokalj, A. *Journal of Molecular Graphics and Modelling* **1999**, *17*, 176–179.

(81) Monkhorst, H. J.; Pack, J. D. *Physical review B* **1976**, *13*, 5188.

(82) Furness, J. W.; Kaplan, A. D.; Ning, J.; Perdew, J. P.; Sun, J. *The journal of physical chemistry letters* **2020**, *11*, 8208–8215.

(83) Poglitsch, A.; Weber, D. *The Journal of chemical physics* **1987**, *87*, 6373–6378.

(84) Hartwigsen, C.; Gœdecker, S.; Hutter, J. *Physical Review B* **1998**, *58*, 3641.

(85) Mosconi, E.; Amat, A.; Nazeeruddin, M. K.; Gratzel, M.; De Angelis, F. *The Journal of Physical Chemistry C* **2013**, *117*, 13902–13913.

(86) Yin, W.-J.; Yang, J.-H.; Kang, J.; Yan, Y.; Wei, S.-H. *Journal of Materials Chemistry A* **2015**, *3*, 8926–8942.

(87) Stranks, S. D.; Eperon, G. E.; Grancini, G.; Menelaou, C.; Alcocer, M. J.; Leijtens, T.; Herz, L. M.; Petrozza, A.; Snaith, H. J. *Science* **2013**, *342*, 341–344.

(88) Xing, G.; Mathews, N.; Sun, S.; Lim, S. S.; Lam, Y. M.; Grätzel, M.; Mhaisalkar, S.; Sum, T. C. *Science* **2013**, *342*, 344–347.

(89) Utsumi, K; Iigusa, H; Tokumaru, R; Song, P.; Shigesato, Y *Thin Solid Films* **2003**, *445*, 229–234.

(90) Koida, T.; Shibata, H.; Kondo, M.; Tsutsumi, K.; Sakaguchi, A.; Suzuki, M.; Fujiwara, H. *Journal of applied physics* **2012**, *111*.

(91) Koida, T. *physica status solidi (a)* **2017**, *214*, 1600464.

(92) King, P.; Lichti, R.; Celebi, Y.; Gil, J.; Vilão, R.; Alberto, H.; Duarte, J. P.; Payne, D.; Egdell, R.; McKenzie, I, et al. *Physical Review B* **2009**, *80*, 081201.

(93) Sommer, A.; Bothschafter, E.; Sato, S.; Jakubeit, C.; Latka, T.; Razskazovskaya, O.; Fattahi, H.; Jobst, M.; Schweinberger, W; Shirvanyan, V., et al. *Nature* **2016**, *534*, 86–90.

(94) Sato, S. A.; Taniguchi, Y.; Shinohara, Y.; Yabana, K. *The Journal of chemical physics* **2015**, *143*.

(95) Otobe, T; Yamagiwa, M; Iwata, J.-I.; Yabana, K; Nakatsukasa, T; Bertsch, G. *Physical Review B* **2008**, *77*, 165104.

(96) Tancogne-Dejean, N.; Mücke, O. D.; Kärtner, F. X.; Rubio, A. *Physical review letters* **2017**, *118*, 087403.

(97) Uemoto, M.; Kurata, S.; Kawaguchi, N.; Yabana, K. *Physical Review B* **2021**, *103*, 085433.

(98) Garg, M.; Kim, H.-Y.; Goulielmakis, E. *Nature Photonics* **2018**, *12*, 291–296.